Physica Scripta

PAPER

Vanadium oxide-based 16 × 16 reflectarray or FSS, reflect-transmitarray and FSS-based Cross-polarized wave absorber for future 6G applications

To cite this article: Ravi Mali *et al* 2025 *Phys. Scr.* **100** 065517

IOP Publishing Phys. Scr. **100** (2025) 065517 https://doi.org/10.1088/1402-4896/add29d

Physica Scripta

RECEIVED
31 January 2025

REVISED
24 March 2025

ACCEPTED FOR PUBLICATION
30 April 2025

PUBLISHED
14 May 2025

PAPER

Vanadium oxide-based 16 × 16 reflectarray or FSS, reflect-transmitarray and FSS-based Cross-polarized wave absorber for future 6G applications

Ravi Mali , Rajkumar Jatav , Praveen Singh Rathore and Manoj Kumar Meshram*

Department of Electronics Engineering, Indian Institute of Technology, Banaras Hindu University, Varanasi, Uttar-Pradesh, (221005), India

* Author to whom any correspondence should be addressed.

E-mail: ravimali.rs.ece24@iitbhu.ac.in, rajkumar.jatav.rs.ece18@iitbhu.ac.in, praveensrathore.rs.ece19@iitbhu.ac.in and mkmeshram.ece@iitbhu.ac.in

Keywords: frequency selective surface, FSS based absorber, polarization rotating unit cell, reflectarray, reflective-transmittive surface, terahertz (THz), VO_2

Abstract

In this paper, a novel unit cell-based array is designed and analyzed using a VO_2-based intelligent ground plane. The proposed array can be used as reflectarray or frequency selective surface (FSS), FSS based cross-polarized wave absorber, and reflective-transmittive surface. The intelligent ground plane is made up of a cross-shaped slot, and it is filled with a thin vanadium dioxide (VO_2) layer. The conductivity of the VO_2 material is temperature-sensitive and it is changed due to the applied external DC biasing. The tunability of VO_2 conductivity introduces the quad-function performance characteristics in a single array at 1–2 THz band. The first application of reflectarray is obtained by high DC (V_1 Volt) biasing, while the other three applications are achieved by low voltage V_2 ($V_2 < V_1$). A polarization rotating unit cell (PRUC) is designed to enhance the bandwidth and to obtain a wide 180° phase shift. This novel compact array saves the cost and area for THz applications. The array consists of 16 × 16 elements which is illuminated by a normal incidence of pyramidal horn antenna. The total volume of the array is $1600 \times 1600 \times 2100\ \mu m^3$. The performance characteristics of the individual unit cell and array with and without intelligent ground plane are simulated in CST Microwave Studio.

1. Introduction

For future 6G communication, various frequency bands are considered in microwave and THz gap as shown in figure 1. In microwave, the mid frequency band is between 7–24 GHz for mega city coverage, W-Band (75–110 GHz), D-Band (110–175 GHz) and the higher frequency band is 275–300 GHz. THz gap covers the frequency range from 0.3–10 THz, and the corresponding wavelength is 1mm to 30 μm [1].

Long-distance 6G communication devices require antennas with high gain, high data rates, directional or bidirectional patterns, frequency, and pattern reconfigurability, wide bandwidth, and a low-profile design. These properties can be achieved through the design of reflectarray, reflect-transmitarray, and transmitarray antennas, which offer the flexibility and performance needed for advanced 6G systems. These antennas allow efficient beamforming, high data throughput, and adaptability across different frequency bands, making them ideal for long-range, high-frequency communication.

Reflectarray is the surface that reflects and collimates the beam of the incident electromagnetic wave. The phase of the reflected wave is the function of the patch size, which was characterized by infrared interferometer. In literatures, various geometries of the unit cell and array were proposed for THz wave applications [2–23]. Ginn *et al* [2] presented the first reflectarray demonstrations at 28.3 THz. This was fabricated by using electron beam lithography. Daniel *et al* [3], present the theoretical and experimental analysis of reflectarray and normal

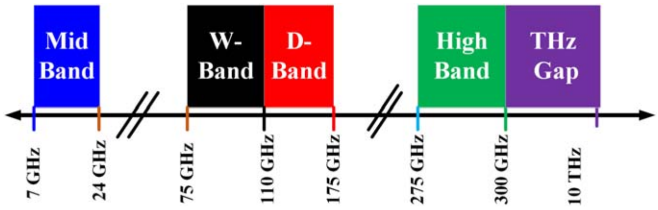

Figure 1. 6G spectrum band.

metasurface at 1 THz. It is highlights that the use of dielectric resonators in terahertz reflectarray antennas leads to significant efficiency improvements compared to metallic resonators. The Graphene-based reflectarray [4], OAM vortex wave generation reflectarray [5–7], was designed at THz frequencies. In graphene-based reflectarray [4–7], the surface impedance can be controlled by changing the chemical potential of the graphene material by applying external DC voltage. Meng *et al* [8] was designed an electronically reconfigurable liquids crystal based reflectarray for beam scanning, 6G beam forming, and beam splitting in the W-band. In [9], a high aperture efficiency 2D beam-scanning liquid crystal-embedded reflectarray antenna was designed for 6G FR3 and radar applications. However, in conventional feed reflectarray antennas, radiation efficiency and gain are often low due to feed blockage. As a result, designing a reflectarray with high gain and high efficiency at GHz and THz frequencies presents significant challenges. Various literatures have reported to mitigate the effect of feed blockage by changing the normal feed to offset feed [10], and replacement of horn antenna with planar log periodic antenna [11], spoof surface plasmon polaritons based low profile endfire MIMO antenna [12], high gain antipodal Vivaldi antenna [13]. This inspired the researchers to design a transmitarray antenna aimed at achieving high gain and high efficiency for future wireless applications.

In [14], a graphene-based circularly polarized transmitarray antenna was proposed. In [15], a metallic waveguide-based dual-band, multi-beam transmitarray was presented for THz applications. Both reflectarray and transmitarray antennas were single-direction antennas. To achieve transmission as well as reflection, the surface was replaced manually according to the applications. To design a surface that has multifunction transmission and reception at the same frequency, called a reflect-transmitarray antenna. Designing of a bi-functional multibeam, low-cost reflect-transmitarray antenna for THz communications by using the tunability of graphene conductivity was reported in [16]. Recently, it has been seen that apart from reflection, transmission, and reflection-transmission, the absorption and FSS properties are also considered for various applications [17–24]. In [17], a THz metasurface was developed for absorber or reflectarray applications. The absorber or a reflectarray were designed by two types of unit cells with low or high reflectivity. The absorption of −10 dB was achieved in the 0.102 THz band, while the reflectarray gain reaches to 22.5 dBi at 0.875 THz. In [18], a broadband switchable metamaterial absorber with multi-laps graphene sheets was designed at a THz frequency band. The absorber can be switched from absorption (>90%) to reflection (>93%) over a broadband range by using the ion-gel top gate method. Further, the FSS at GHz and THz band is also been subjected to numerous scientific studies [19–22]. The FSS designed using Babinet's principle, where the conducting layer was designed on the top of the substrate, and a complement of different slot etched on either side of the substrate, acronym as complementary frequency selective surfaces (CFSS), which produces two narrow transmission bands separated with a stop band [19]. In [21], a self-complementary Jerusalem cross metasurface-based FSS is designed at a multiband THz regime. In [22], a Jerusalem cross FSS element and equivalent circuit model with a transmission line model were discussed for effective electromagnetics (EM) shielding applications. Recently, it is observed that the dual band FSS was used to design microwave absorber, since this type of design provide intelligent shielding which absorb only the desired frequency band and became transparent to other frequency bands [23, 24].

Now a day, researchers are interested in artificial metasurface, which provides more than one application in a single array structure. It is possible by the utilization of thin layer of graphene and VO_2 film. From the last decade, various literatures have been reported based on the graphene sheet and VO_2 film due to the nature of tunability of the conductivity of both materials. Recently, various VO_2 based metasurface was designed for absorbers, polarization converters, dual function switching [25–27] and [28], and graphene-based antenna loaded with metasurface at THz regime [29–34]. In [35], VO_2 based reconfigurable reflectarray antenna was designed at 1.1 THz for beam scanning up to 100°.

The conductivity of the graphene material is tuned by changing the chemical potential, while the VO_2 film conductivity is temperature-dependent. Note that the transition in properties of VO_2 remains unclear. It may be caused by joule heat [36, 37] or electric current [38, 39]. This temperature is changed with an applied DC biasing. Except the graphene material, VO_2 is another kind of existing material which is having two transition states

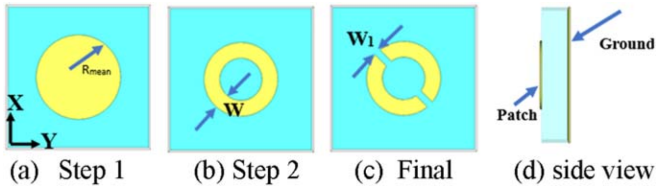

Figure 2. Design evaluation of the unit cell.

(insulating and metallic state). When VO_2 is in an insulating state, the dielectric constant and conductivity are 9 and 200 S m^{-1}, respectively. The permittivity of VO_2 is characterized by the Drude model [40] in the metallic state using equation (1).

$$\varepsilon(\omega) = \varepsilon_\infty - \frac{\omega_p^2(\sigma)}{\omega^2 - i\gamma\omega} \tag{1}$$

Where, the permittivity at high frequency of the material ε_∞ is 12, collision frequency (γ) is 5.75 $\times$ 10^{13} rad/s, the plasma frequency (ω_p) for gold is 1.67 $\times$ 10^{15} rad and calculated by using [27]

$$\omega_p^2(\sigma) = \frac{\sigma}{\sigma_o}\omega_p^2(\sigma_o) \tag{2}$$

at conductivity ($\sigma = 2 \times 10^5$ S/m at the above temperature (T > 341.15 K) [41].

In this paper, we propose a novel unit cell-based array by using a VO_2 based intelligent ground plane to achieve quad-functions as reflectarray, frequency selective surface, FSS based cross polarized wave absorber and reflective-transmittive surface at THz regime. A VO_2 film is used to transform the performance of reflectarray to FSS, absorber and a dual-band reflection-transmission. A polarization rotating unit cell (PRUC) for wide band mm-wave application was defined in [42]. The proposed unit cell without an intelligent ground plane provides a wide band reflective surface with a bandwidth of 0.69 THz. A cross slot is etched on the ground plane of the proposed unit cell, functioning as a frequency selective surface (FSS) with two narrow transmission bands separated by a wide stop band. The transmission bands are TB1 (1.08–1.38 THz) and TB2 (1.87–2.2 THz), with the stop band covering the range of 1.38–1.87 THz. A VO_2 film is introduced on the ground cross shaped slot to make it as an intelligent ground plane. When the VO_2 film is in its conducting state, the array act as a reflectarray. The nature of the reflecting element and array can be transformed from reflectarray to FSS, cross polarized wave absorber and reflective-transmissive surface when VO_2 film acts as an insulating state. The array is illuminated by a pyramidal horn antenna of 13 dBi gain. The response has been simulated and studied for all the four applications in CST Microwave Studio-2024.

2. Unit cell design and methodology

The design of the proposed wide band reflectarray is a four-step process as shown in figure 2. In the first step, targeted frequency bands of interest at 1.3 THz are chosen. To achieve a reflection band over the targeted frequency range, the concept of ring resonator is utilized, whose fundamental frequency is given by

$$f_0 = \frac{C}{l_{mean}\sqrt{\varepsilon_{eff}}} \tag{3}$$

where $l_{mean} = 2\pi R_{mean}$. l_{mean}, R_{mean} are mean length and mean radius of the ring, respectively. ε_{eff} is the effective permittivity of the metasurface within stratified media [43]. So, we have chosen the annular ring too achieve the reflection at 1.3 THz.

$$\varepsilon_{eff} = \varepsilon_r + (1 - \varepsilon_r)e^{-\alpha\left(\frac{d}{D}\right)} \tag{4}$$

where a is the shape factor, d is the thickness off the substrate, D is the periodicity of the unit cell.

The design of the unit cell has three steps.

Step 1, the radius of the circular ring can be introduced by using equations (3) and (4). The radius of the circular patch is 26 μm, resulting in a total mean length of 188 μm. The substrate thickness is 20 μm, and the unit cell periodicity is 100 μm. The calculated effective permittivity is 1.65, obtained using equation (3). The resonant frequency is determined using equations (3) and (4). The obtained calculated first resonant frequency is 1.24 THz, while the simulated the first resonant frequency is 1.30 THz and second harmonic is at 2.08 THz. the simulated reflection magnitude of step 1 and 2 is depicted in figure 3(a). To enhance the bandwidth in final step, a rectangular slit is etched on the circular patch which is produced a wide band which is shown in figure 3(b)

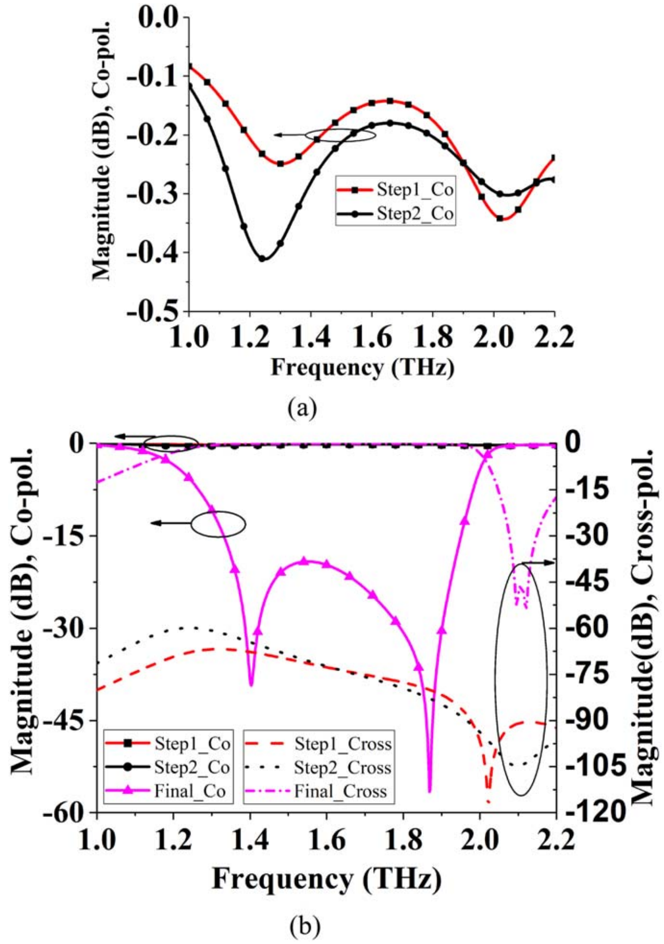

Figure 3. (a) Reflection magnitude of stages 1 and 2. (b) the magnitude of the co and cross-polarized reflection coefficient of the proposed stages.

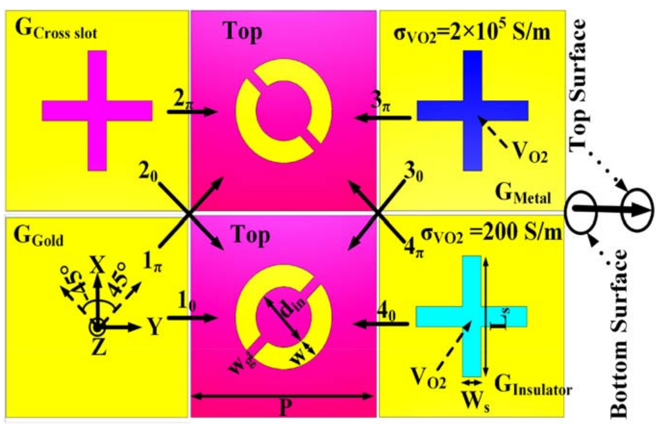

Figure 4. Top and bottom view of the proposed unit cell in various stages.

The schematic view of the proposed unit cell for various stages, such as reflective surface, FSS, FSS based cross polarized wave absorber and reflective-transmittive surface with and without an intelligent ground plane is depicted in figure 4. The unit cell is designed by sandwiching the substrate (SiO_2, $\varepsilon_r = 3.9$, $\tan\delta = 0.001$) with top metallic split ring (Gold) and bottom ground plane (Gold). The periodicity (P) of the unit cell is 100 μm, the thickness of the substrate is 20 μm, and the thin metallic ring and the ground plane is 1 μm. The radius of the inner ring is 15 μm, and the width of the split ring is 1μm. The polarization is converted by etching the slot diagonally. The width of this slot is 5 μm. This slot is cut along XY-axis by ±45°. The unit cell has 2 states: 0-state

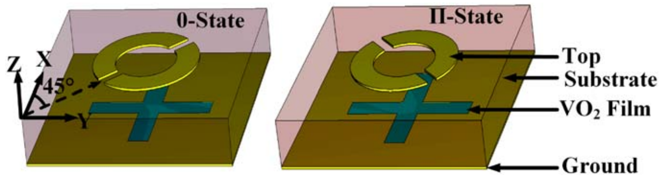

Figure 5. Perspective view of the proposed unit cell with intelligent ground plane.

and π-state. The reflection phase difference of 180° is obtained between both states. The unit cell with the slot in 45° along X-axis is considered as 0-state, while the slot in −45° along X-axis is considered as π-state.

Figure 4 consists of 4 various stages with 8 combinations. Each stage has two combinations, which is depicted by $1_{0,\pi}$, $2_{0,\pi}$, $3_{0,\pi}$, $4_{0,\pi}$. In figure 4, the arrowhead represents the top view of the unit cell and the tail of the arrow shows the bottom view of the proposed unit cell. Stages $1_{0,\pi}$, $2_{0,\pi}$ are designed without an intelligent ground plane, while $3_{0,\pi}$, $4_{0,\pi}$ is designed with intelligent ground plane. Stage 1_0 and stage 1_π, both have fully metallic (Gold) ground planes. While in stage 2_0 and stage 2_π, a cross-shaped slot is etched on the ground plane. The length of the cross-shaped slot L_s is 60 μm, and the width W_s is 10 μm. In stages $3_{0,\pi}$ and $4_{0,\pi}$, the cross-shaped slot in the ground plane is filled with temperature-dependent vanadium oxide (VO_2) material film. Due to the temperature-dependent characteristics, the conductivity (σ) of the material is changed and the ground plane works as an intelligent ground surface. When the temperature is below 341.15K, the conductivity of VO_2 is < 200 S m^{-1}, and it works as an insulator. While, if the temperature is above 341.15 K, the film conductivity is very high about 2×10^5 S m^{-1}, which means it is working as a highly conductive metal. The temperature-dependent conductivity of this material is defined by the Drude model [36]. The intelligent ground plane is used to obtain the various properties such as reflection or FSS, cross polarized wave absorber, and reflective-transmittive surface in a single unit cell. In figure 4, stage $3_{0,\pi}$, shows the VO_2 film works as a high conductivity metal at a temperature above 341.15K, while in Stage $4_{0,\pi}$, it shows the VO_2 film works as an insulator at a temperature below 341.15K. The proposed stages are simulated with $E_t = 0$ and $H_t = 0$ boundaries in X- and Y-direction, and open (add space) is assigned along $\pm Z$-axis with two waveguide ports applied along $\pm$ Z direction from the deemed distance of the surface is 50 μm. This simulated setup is the same for all stages. In stages 1 and 3, the ground plane works as a highly conductive metal, so that the transmission is zero, while for stages 2 and 4, the ground plane works as an open/insulator, so some transmissions exist. The previously reported literature [19–22] presented a dual-band transmission which is separated by a stop band by designing a complementary frequency selective surface (CFSS). Similar to the stages 2 and 4, due to the cross slot on the ground plane and VO_2 film act as an insulator and the unit cell works as a dual-band frequency selective surface with wide band rejection.

In section II(A), stages 1 and 3 reflectarray unit cell performance characteristics is elaborated. In section II(B), the FSS performance characteristics explained for stage 2 and 4 as well as the effect of the cross slot is also compared for stages 1,2,3,4. In section II(C), the reflection-transmission characteristics performance is described for stage 2 and 4. The perspective view of the final proposed unit cell with intelligent ground plane is shown in figure 5.

2.1. Polarization rotating unit cell (PRUC) for RA

This section describes the performance characteristics of a wideband polarization rotating unit cell with a fully backed ground plane. Figure 6 depicts the magnitude and reflection phase characteristics of the reflective EM wave for PRUC stage$1_{0,\pi}$. The PRUC provides the magnitude of the co-polarization reflection coefficient $R_{xx} < -10$ dB, and the cross-polarization reflection coefficient $R_{yx} > -0.8$ dB for both stages 1_0 and 1_π. The operating band covers the frequency range from 1.29 THz to 1.98 THz. Stages 1_0 and 1_π produces a 180° phase difference for cross-polarization reflection coefficients over the frequency range from 1 to 2 THz, which is responsible for PRUC to act as a wideband phase shifter. While, for the co-polarization reflection coefficient, there is a 0° phase difference, which means the co-polarization coefficient parameters is not contributing for the reflection of the wave. The vector surface current distribution for stage 1_0 and 1_π at 1.4 THz is depicted in figures 7(a) and (b). As shown in figures 7(a) and (b), the surface current ($\vec{s}_1$ and $\vec{s}_2$) flows in the same direction along both arms of the split ring resonator, which works as a cut wire resonator [38, 39] at 1.4 THz and 1.89 THz with resultant current on top surface arms (J_{T0} and $J_{T\pi}$) along the XY plane. In addition to that, the induced surface current (J_{G0} and $J_{G\pi}$) along the ground plane is antiparallel to the resultant current (J_{T0} and $J_{T\pi}$) of the arms. This antiparallel surface currents produces two resonances at 1.4 THz and 1.89 THz. Due to this multiple magnetic resonance a wide bandwidth is obtained from 1.29 THz to 1.98 THz.

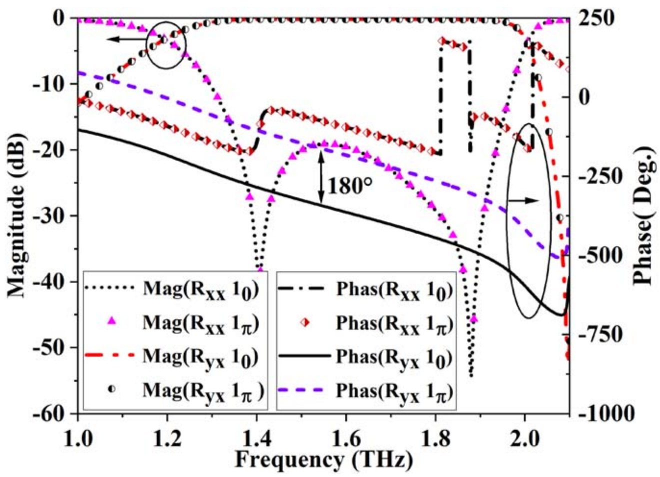

Figure 6. Simulated co- and cross-polarization reflection coefficients magnitude and phase characteristics for stage $1_{0,\,\pi}$.

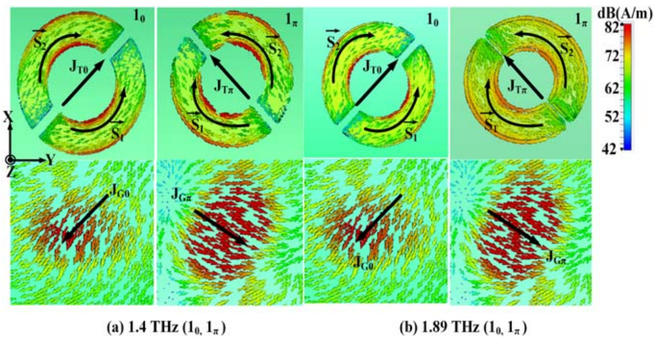

Figure 7. Vector surface current distribution at (a) 1.4 THz (1_0,1_π), and 1.89 THz (1_0,1_π).

2.2. Frequency selective surface (FSS)

In [19–22], the FSS works as a spatial filter, which is used for selective transmission of specific frequency bands, while rejecting others in the microwave, millimeter wave, and THz-gap. This section describes the performance characteristics of a wideband polarization rotating unit cell with a cross-shaped slot-backed ground plane. Figure 8 depicts the magnitude and reflection phase characteristics of the incident EM wave for (FSS) stage $2_{0,\,\pi}$. The FSS provides the magnitude of the co-polarization reflection coefficient in reflection band RB_1 and RB_2 with $R_{xx} < -10$ dB, while stop band with $R_{xx} > -1$dB, for both stages 2_0 and 2_π. From figure 8, it is observed that the FSS produces 0° phase difference for the co-polarization reflection coefficient in the overall frequency band from 1 to 2.2 THz, which is not responsible for the reflective nature of the unit cell (FSS). The FSS provides the magnitude of the cross-polarization coefficient in reflective bands RB_1 and RB_2 is $R_{yx} > -1$ dB, while in stop band a prominent dip can be observed at 1.71 THz with $R_{yx} < -10$ dB for both stages 2_0 and 2_π. The FSS produces 180° phase difference and $R_{yx} > -1$ dB in both bands RB_1 and RB_2, which is responsible for reflective nature. Whereas in stop band the $R_{yx} < -10$ dB, which is responsible for the absorption of the cross polarized wave.

Figure 9 depicts the magnitude and phase characteristics of the transmitted EM wave for FSS in transmission mode of stage $2_{0,\,\pi}$. The FSS provides the magnitude of the maximum co-and cross-polarization transmission coefficient in transmitted frequency $T_{F1} = 1.31$ THz is (0.38 ,0.26) and at $T_{F2} = 2.06$ THz is (0.36 and 0.38) respectively. While in stop frequency $S_{F1} = 1.71$ THz is (0.44 and 0.035) for both stages 2_0 and 2_π. In figure 9, it is observed that the FSS produces 0° phase difference for the co-polarization transmission coefficient in the overall frequency band from 1 to 2.2 THz, which is not responsible for the transmission. However, The FSS produces 180° phase difference for both transmission frequencies, which is responsible for transmission of cross polarized wave, while it fluctuates in the stop band so there is no transmission in cross polarized wave while it is absorbed in this band. The absorption characteristics of the cross polarized wave is described in next subsection C. Figure 10, shows the comparison performance of the polarization reflective unit cell and polarization rotating FSS of stage $1_{0,\,\pi}$ and stage $2_{0,\,\pi}$, respectively.

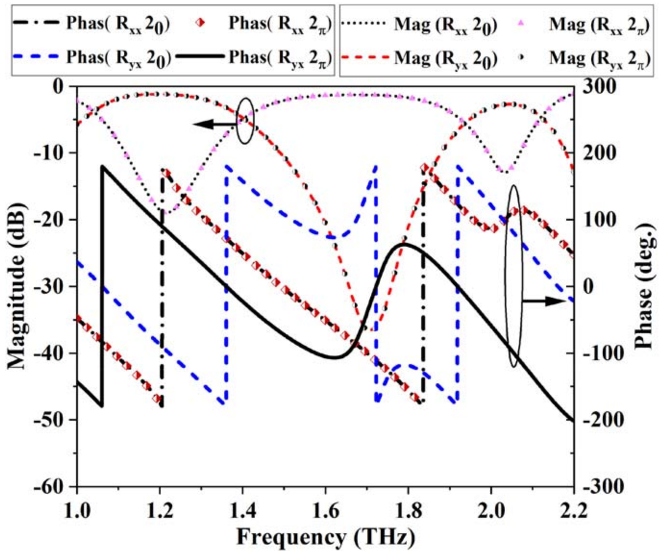

Figure 8. Simulated magnitude and phase characteristics co- and cross-polarization reflection coefficients for stage $2_{0,\pi}$.

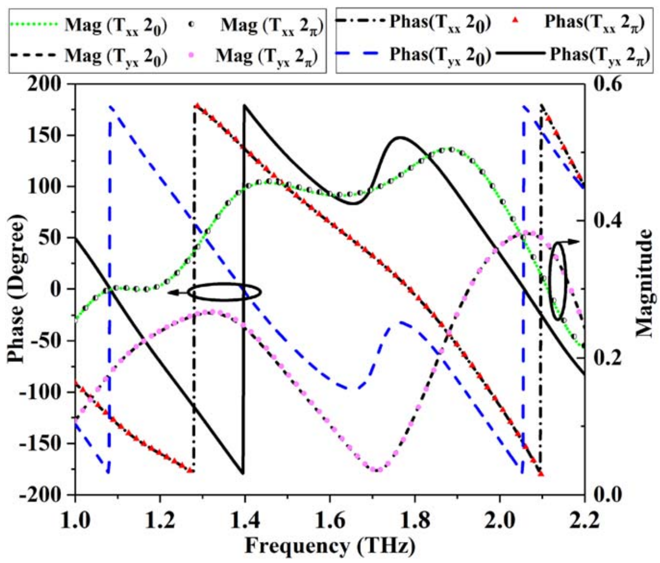

Figure 9. Simulated magnitude and phase characteristics of co- and cross-polarization transmission coefficients for stage $2_{0,\pi}$.

In stage 2, there are two narrow transmission bands exists, which are separated by a wide stop band. The transmission frequencies TF_1 and TF_2 are 1.31 THz and 2.06 THz, and the stop band is 1.4 THz to 1.97 THz. From figure 10, it is observed that the reflective response ($1_{0,\pi}$) of the unit cell can be converted into the band rejection and the transmittive response in ($2_{0,\pi}$) is obtained by etching a cross-shaped slot on the ground plane.

2.3. Cross polarized wave absorption in FSS

The absorptivity of a metal backed absorber can be calculated by equation (5), .44.

$$\mathrm{A}(\omega) = 1 - |R(\omega)|^2 \tag{5}$$

while, the absorptivity of the frequency selective surface unit cell is calculated by equation (6) [24]

$$A(\omega) = 1 - |R(\omega)|^2 - |T(\omega)|^2 \tag{6}$$

where $|R(\omega)|^2 = |R_{xx}(\omega)|^2 + |R_{yx}(\omega)|^2$ characterized the reflected power from the unit cell, and $|T(\omega)|^2 = |T_{xx}(\omega)|^2 + |T_{yx}(\omega)|^2$ is the transmitted power from the unit cell. R_{xx}, R_{yx}, T_{xx}, T_{yx} is the co and cross polarized reflection and transmission coefficient of the reflected and transmitted EM wave from the unit cell. In this proposed work the x (or TE)- polarized wave is incident on the surface of unit cell, which is reflected

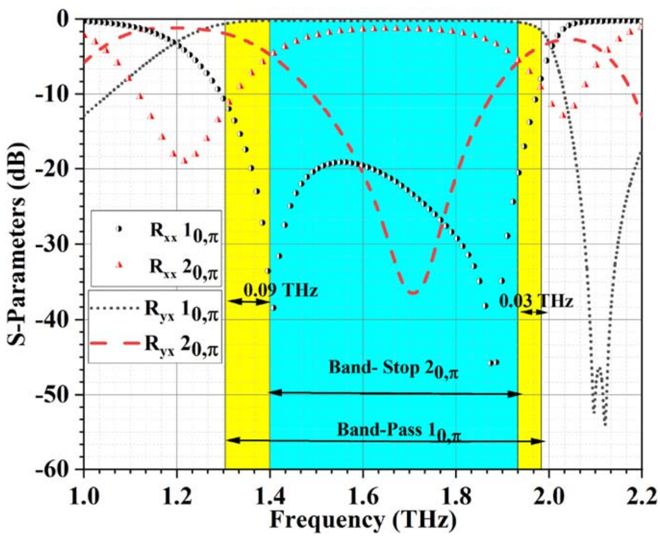

Figure 10. Simulated co- and cross-polarization reflection coefficients magnitude characteristics for stage $1_{0,\pi}$ and stage $2_{0,\pi}$.

and transmitted due to the slot ring on the top patch and ground slot. The reflected and transmitted waves are represented in term of electric field.

$$|R_{xx}(\omega)| = \frac{|\vec{E}_{rx}{}^{Abs}|}{|\vec{E}_{ix}{}^{Abs}|} \tag{7}$$

$$|R_{yx}(\omega)| = \frac{|\vec{E}_{ry}{}^{Abs}|}{|\vec{E}_{ix}{}^{Abs}|} \tag{8}$$

$$|T_{xx}(\omega)| = \frac{|\vec{E}_{tx}{}^{Abs}|}{|\vec{E}_{ix}{}^{Abs}|} \tag{9}$$

$$|T_{yx}(\omega)| = \frac{|\vec{E}_{ty}{}^{Abs}|}{|\vec{E}_{ix}{}^{Abs}|} \tag{10}$$

The previously reported literature [44–48] used equation (5) to calculate the actual absorption power of a polarized rotating unit cell with backed ground plane. In [24], the absorption power was calculated for FSS unit cell by using co- and cross polarized coefficient of reflected and transmitted wave using equation (6). Based on the previous reported literature, we have calculated the absorptivity by using co- and cross-polarized reflection and transmission coefficient of the unit cell, which is depicted in figure 11. The absorption of the reflected and transmitted co-polarized wave is more than 87% at 1.2 THz and 80% at 2.05 THz, while the absorption of the co-polarized wave in stop band is 10% at 1.7 THz. The absorption of the cross-polarized wave is above 20% at 1.2 THz and 30% at 2.05 THz, while the absorption of the cross polarized wave in stop band is about 100% at 1.7 THz. In this work, we have also calculated the absorption by using both co- and cross-polarized reflected and transmitted wave. The absorption is below 10% when considering both transmission as well as reflection of co-cross polarized wave. So, it is evident from figure 30, if the array is designed by using the cross polarized phase characteristics and the array is illuminated by space feed, then the incident cross polarized wave power can be absorbed in stop band. While, it transmit-reflect at 1.2 THz and 2.05 THz. The above discussion of absorption is validated in section IV. The array design is described by using the phase characteristics of the cross polarized EM wave. In the results section, figure 30, it is confirmed that the cross-polarized wave power is absorbed in the stop band while the reflection and transmission is obtained at 1.2 and 2.05 THz.

In stop band, the unit cell characteristics of the cross-polarized reflection coefficient provides the absorption, and the unit cell is working as a polarizer-based absorber47. The cross-shaped slot provides good band rejection between the transmission band at 1.2 THz and 2.05 THz and provides transmittive as well as reflective nature at respective frequency.

The performance response of the reflective-transmittive surface for stage 2_0 and 2_π is described in section II (C). The top and bottom view of the vector surface current distribution for stage 2_0 and 2_π at 1.2 THz and 2.05 THz is depicted in figures 12(a) and (b).

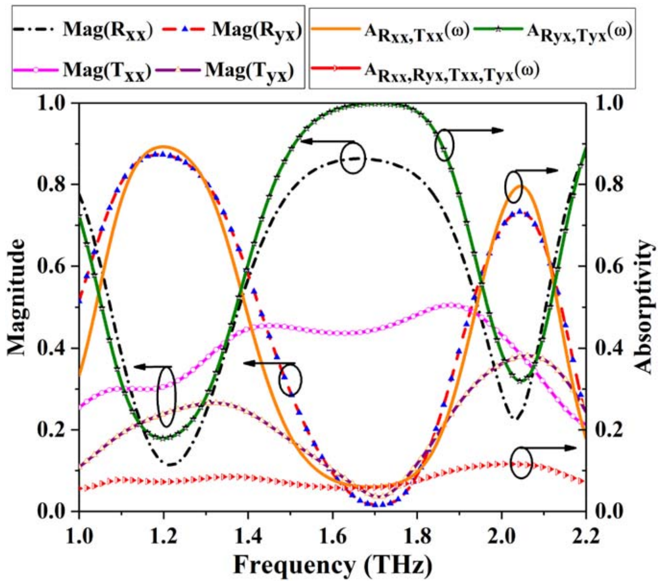

Figure 11. Simulated absorption of the proposed unit cell (FSS).

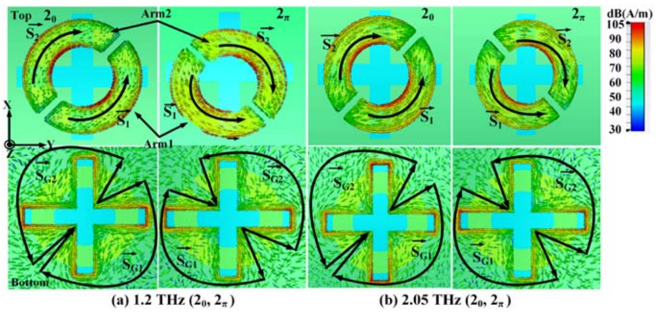

Figure 12. Vector surface current distribution for stage 2_0 and 2_π at (a) 1.2 THz (b) 2.05 THz.

It is observed that, in each unit cell, there are two surface currents ($\vec{s}_1$ and $\vec{s}_2$) are flowing along the direction of arrow in Arm1 and Arm2 due to normal incidence of EM wave. In addition to that, there are two surface currents ($\vec{s}_{G1}$ and $\vec{s}_{G2}$) induced in the defective ground plane opposite to the current flow in the arms. This anti-parallel surface currents makes magnetic dipole resonance which produces reflection as well as transmission at 1.2 THz and 2.05 THz.

2.4. Reflective-transmittive surface

In this section, the nature of the reflection-transmission characteristics of stage 2 is described. In figure 13, the cross-polarization reflection-transmission magnitude and phase characteristics of the proposed unit cell are depicted. The reflection and transmission magnitude of the cross-polarized wave at 1.2 THz is 0.87 and 0.23 with 180° phase difference, while at 2.05 THz is 0.73 and 0.37 with 180° phase difference. In stop band, at 1.7 THz the magnitude is 0.01 and 0.03 with fluctuation in the phase.

In stage 2, the unit cell element is illuminated by a x (TE)-polarized EM wave. The cross-polarized field component of the reflected wave and transmitted wave exists along the y-direction, which is defined by R_{yx} and T_{yx}, respectively.

$$R_{yx} = \frac{E_{yr}}{E_{xi}} \tag{11}$$

$$T_{yx} = \frac{E_{yt}}{E_{xi}} \tag{12}$$

In section II, the sections A, B, C and D explained the performance characteristics of the unit cell element in stage 1 and stage 2, and are utilized as a reflectarray, frequency selective surface, absorption and transmit-reflect

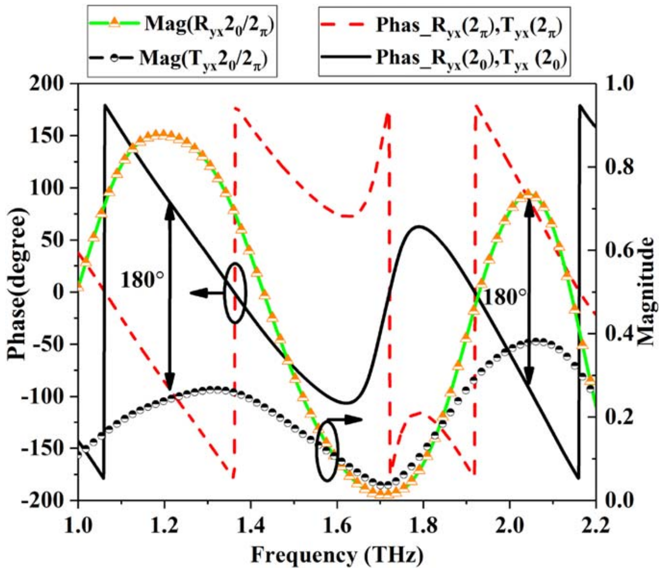

Figure 13. Simulated magnitude and phase characteristics for reflective-transitive nature of stage $2_{0,\pi}$.

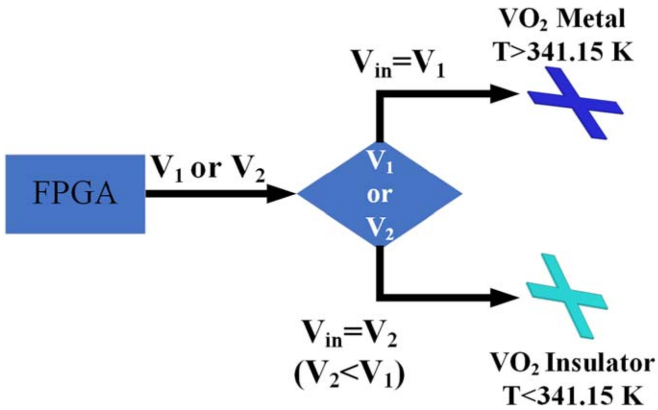

Figure 14. Schematic view of the biasing representations of the VO_2 film.

array, respectively. It is observed that the reflectarray will be designed by utilization of stage $1_{0,\pi}$ unit cell, which should have a full ground plane at the bottom side of the substrate. Transmit-reflectarray, FSS and cross-polarized wave absorber will be designed using the stage $2_{0,\pi}$ unit cell, which has a cross-shaped slot ground plane at the bottom side of the substrate. It is concluded that, for different applications, we utilized separated stages of unit cells. The applications of both stage unit cells are illustrated in section IV. It is observed that it is very difficult to manually replace the unit cell ground plane for different space applications. So, the authors' provide a solution in this paper. All four applications are possible using a single intelligent ground plane. The solution is possible by filling the cross-shaped VO_2 film on the cross-shaped slot ground plane in stage 2. The VO_2 has dual properties which is depends on the temperature. If the temperature is below 341.15 K, the VO_2 film acts as an insulator, while if the temperature is above 341.15 K, the VO_2 film acts as a high-conductive metal film. These properties are utilized to design an intelligent ground plane for all four applications. The biasing representation of the VO_2 film is depicted in figure 14. It is shown that the dynamically controlled film characteristics by applying the external DC voltage (V_{in}) through field programmable gate array (FPGA) results metal-insulator transition of VO_2. It is observed that if the film voltage is high (V_1 volt), the film acts as metal, while if the voltage is low ($V_2 < V_1$ volt), the film acts as an insulator. In stage 3, the cross-shaped VO_2 film acts as a conductive metallic sheet, while in stage 4, the cross-shaped VO_2 film works as an insulator sheet. The performance characteristics of both stages 3 and 4 are illustrated in section III (A).

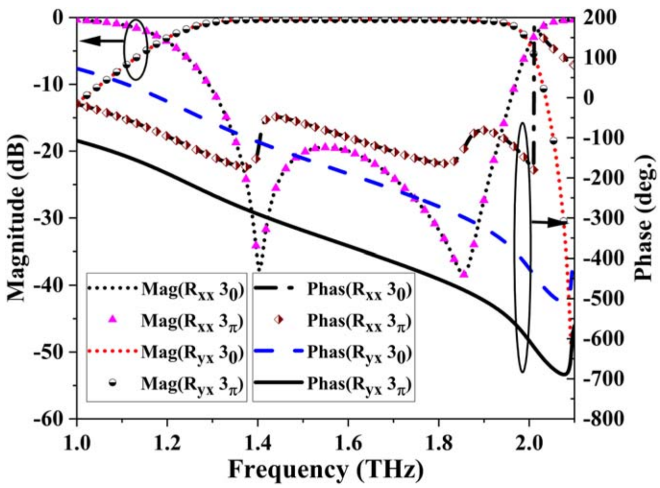

Figure 15. Magnitude and reflection phase characteristics of the stage 3.

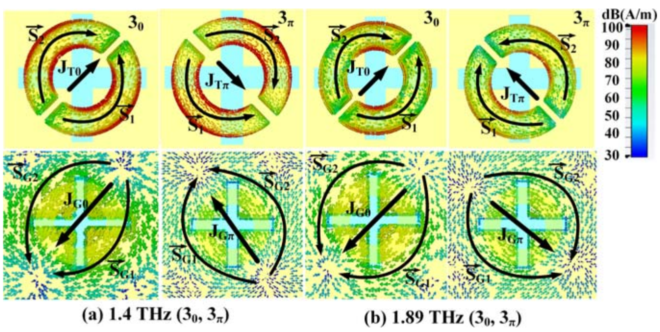

Figure 16. Vector surface current distribution at 1.4 THz and 1.89 THz for Stage (a) 3_0 and (b) 3_π.

3. Intelligent ground plane

3.1. VO_2 film-based reflective unit cell

This section illustrates the characteristics response of the stage $3_{0,\,\pi}$ unit cell in which the cross-shaped slot on the ground plane is filled with VO_2 film. In this stage, the film is excited with required V_1 voltage, due to which it works as a high conductive ($\sigma = 2 \times 10^5$ S m^{-1}) metallic sheet. That means the total ground plane acts as a fully metallic sheet and the resultant response characteristics are similar to reflectarray unit cells as stage 1. The response characteristic of stage 3 is shown in figure15. The magnitude of the co-polarization reflection coefficient is $R_{xx} < -10$ dB, and the cross-polarization reflection coefficient is $R_{xy} > -0.7$ dB for stages 3_0 and 3_π. The operating band covers the frequency range from 1.29 THz to 1.98 THz. Stage 3_0 and 3_π produce a 180° phase difference for cross-polarization reflection coefficients over the frequency range from 1 to 2 THz, which is responsible for acting as a reflecting unit cell, while 0° phase difference for the co-polarization reflection coefficient. The co-polarization coefficient parameters are not suitable for the reflective nature of the wave. The vector surface current distribution for stage 3_0 and 3_π at 1.4 THz and 1.89 THz is depicted in figures 16(a) and (b).

The vector surface current ($\vec{s}_1$ and $\vec{s}_2$) flows in the same direction along both arms of the split ring resonator, which works as a cut wire resonator [42] at 1.4 THz and 1.89 THz with resultant current J_{T0} and $J_{T\pi}$ along the XY-plane. In addition, the induced surface current J_{G0} and $J_{G\pi}$ along the ground plane is antiparallel to the resultant current (J_{T0} and $J_{T\pi}$) of the arms. This antiparallel surface current produces two resonances at 1.4 THz and 1.89 THz. Due to this magnetic resonance the working band is obtained from 1.29 THz to 1.98 THz.

3.2. VO_2 film-based FSS unit cell

This section illustrates the characteristics response of the stage $4_{0,\,\pi}$ unit cell in which the cross-shaped slot on the ground plane is filled with VO_2 film. The applied external required voltage is ($V_2 < V_1$). The VO_2 film acts as an

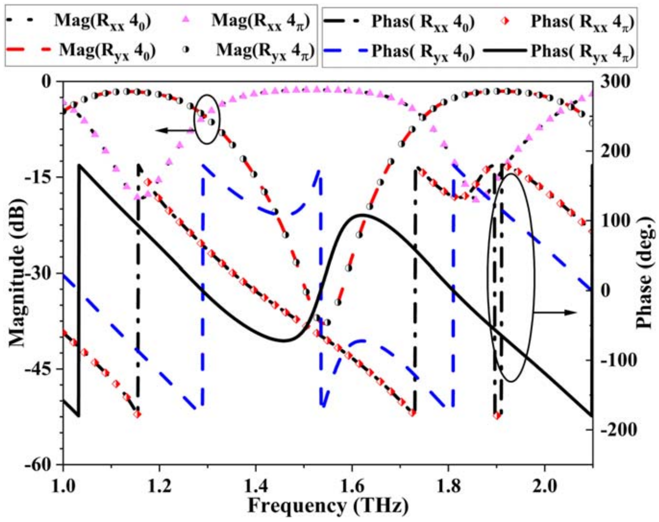

Figure 17. Simulated magnitude and phase characteristics of co- and cross-polarization reflection coefficients for stage $4_{0,\,\pi}$.

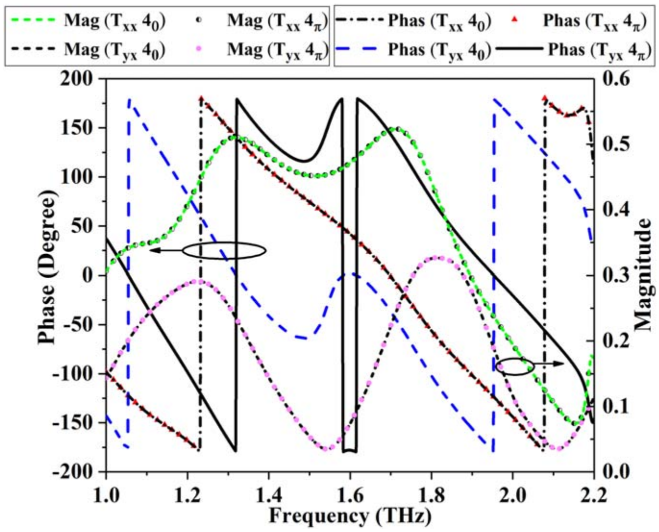

Figure 18. Simulated magnitude and phase characteristics of co and cross-polarization transmission coefficients for stage $4_{0,\,\pi}$.

insulator with low conductivity ($\sigma < 200$ S m^{-1}), and the resultant unit cell response produced two narrow transmission bands which is separated by a wide stop band. This unit cell acts as an FSS. The reflection magnitude and phase characteristics of the reflective electromagnetic wave for (FSS) in stage $4_{0,\,\pi}$ is shown in figure 17. The FSS provides the magnitude of the co- and cross polarized reflection coefficient in band RB_1 (1.08 to 1.29 THz) and RB_2 (1.81 to 2.2 THz) with $R_{xx} < -10$ dB, while in stop band (1.29–1.81 THz) with $R_{yx} > -1.07$ dB, for both stages 4_0 and 4_π. It is observed that the FSS produces 0° phase difference for the co-polarization reflection coefficient in the overall frequency band 1 to 2 THz, which is not responsible for the reflective-transmittive nature of the unit cell (FSS).

The FSS provides the magnitude of the cross-polarization coefficient in band RB_1 and RB_2 is $R_{yx} > -1$ dB, while in stop band $R_{yx} < -10$ dB for both stages 4_0 and 4_π. The FSS produces 180° phase difference for both bands RB_1 and RB_2, which is responsible for reflective nature, while it fluctuates in the stop band. Figure 18 depicts the magnitude and phase characteristics of the transmitted EM wave form (FSS) in transmission mode of stage $4_{0,\,\pi}$. The FSS provides the magnitude of the maximum co- and cross-polarized transmission coefficient in transmitted frequency $T_{F1} = 1.22$ THz is (0.44, 0.29) and at $T_{F2} = 1.81$ THz is (0.44, 0.32) while in stop frequency $S_{F1} = 1.54$ THz is (0.45, 0.03) for both stages 4_0 and 4_π. The FSS produces 0° phase difference for the co-polarization transmission coefficient in the overall frequency band from 1 to 2.2 THz, which is not responsible for the transmission. However, The FSS produces 180° phase difference for both transmission frequency which

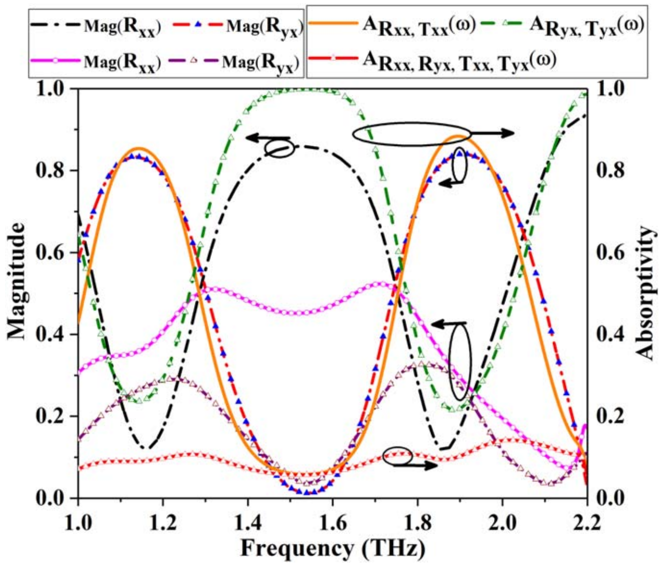

Figure 19. Simulated absorption of the proposed unit cell (FSS) for stage $4_{0,\,\pi}$.

is responsible for transmission of cross polarized wave while it fluctuates in the stop so it is not transmitting the cross polarized wave however it is absorbed in the stop band. The absorption of the cross polarized wave is described in next subsection C.

3.3. VO_2 film-based cross polarized wave absorption

The detailed analysis of the absorption is described in the section II (C). In this section, we calculate the absorption by using co- and cross-polarized reflection and transmission coefficient of stage 4-unit cell, and it is depicted in figure 19. The absorption of the co-polarized wave is about 85% at 1.14 THz and 88% at 1.89 THz, while the absorption of the co-polarized wave in stop band is 5% at 1.53 THz. It is also observed that, the absorption of the cross-polarized wave is about 22% at 1.2 THz and 21% at 1.89 THz, while the absorption of the cross polarized wave in stop band is about 99% at 1.53 THz. In this work, we have also calculated the absorption by using both co- and cross polarized reflected and transmitted wave.

The absorption is below 12% while considering both transmission as well as reflection co-cross polarized wave. So, it is evident that, if the array is designed by using the cross polarized phase characteristics and the array is illuminated by space feed then the incident cross polarized wave power can be absorbed in stop band while it reflect-transmit wave in operating band. The above discussion of absorption is validated in section IV of this proposed work. The array design is described by using the phase characteristics of the cross polarized EM wave and it confirms the absorption in the stop band. In the results section of the array figure 32, it is confirmed that the power is absorbed in stop band while the reflection and transmission is obtained at 1.14 THz and 1.89 THz.

3.4. VO_2 film-based transmit-reflectarray unit cell

In this section, the cross-polarization reflection-transmission coefficients magnitude and phase characteristics of the proposed unit cell are depicted in figure 20. The magnitude of the cross-polarization reflection and transmission coefficient at 1.21 THz, $R_{yx} = 0.76$ and $T_{yx} = 0.24$. while at 1.81 THz the $R_{yx} = 0.73$ and $T_{yx} = 0.27$ and at stop frequency at 1.51 THz the $R_{yx} = 0.01$ and $T_{yx} = 0.04$.

The 180° phase shift is obtained in both bands of cross polarized reflected and transmitted wave cause the possible reflection transmission occurs while it is fluctuating in stop band because there is no reflection and transmission occurred. However, the cross polarized wave is absorbed in this band. In stage 4, the unit cell element is illuminated by a cross-polarized electromagnetic wave. The cross-polarized field components of the reflected wave and transmitted wave exists along the y-direction, which is defined by R_{yx} and $T_{yx,}$ respectively. From section III, it is observed that the unit cell performance characteristics with intelligent ground plane (stage 3 and 4) and without intelligent ground (stage 1 and 2) plane are same. Therefore, the proposed VO_2 film-based ground plane unit cell is utilized for all four applications. The intelligent ground plane-based unit cell is utilized for designing of the reflectarray, FSS, FSS based cross polarized wave absorber and reflective-transmittive surface is illustrated in section IV (B). The vector surface current distribution for stage 4_0 and 4_π at 1.15 THz and 1.85 THz are depicted in figures 21(a) and (b). It is observed that, in each unit cell, there are two surface currents ($\vec{s}_1$ and $\vec{s}_2$) are flowing along the direction of arrow in Arm1 and Arm2 due to normal incidence.

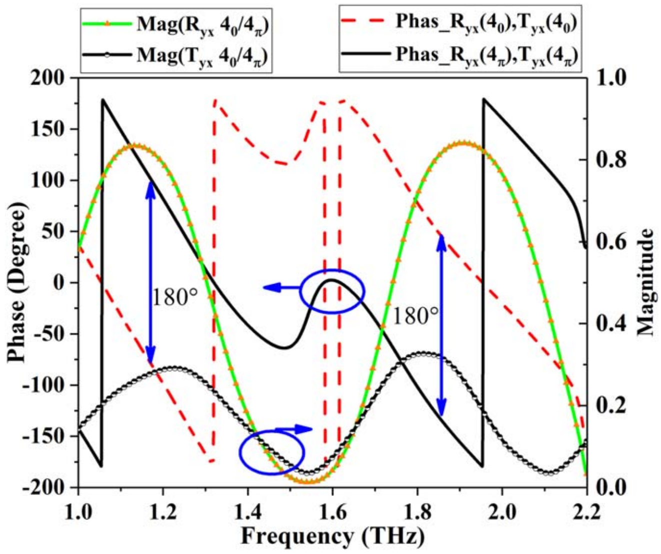

Figure 20. Magnitude and phase plot for reflection-transmission of the stage 4.

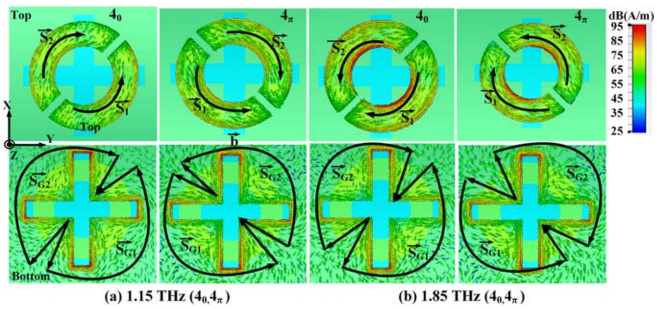

Figure 21. Vector surface current distribution for stage 4 at (a) 1.15 THz (b) 1.85 THz.

In addition to that, there are two surface currents ($\vec{s}_{G1}$ and $\vec{s}_{G2}$) induced in the defective ground plane opposite to the current flow in the arms. This anti parallel surface currents makes magnetic dipole resonance. Which produces transmission at 1.15 THz and 1.85 THz.

4. Array design

4.1. Array performance analysis

We have analyzed the array performance from the unit cell to the full array design, focusing on the effects of mutual coupling and edge effects. As referenced in49–51 array mutual coupling between elements can be understood by analysing the electric field, surface current, and far-field patterns as shown in figures 22(a) to (i).

We have examined the electric field, surface current distribution and far-field characteristics for each possible combination of unit cells in the array design at frequency of 1.5 THz . We specifically analysed the impact on the electric field distribution when unit cells of the same type (0-state or π-state) were placed adjacent to each other, as well as when different states (0-state and π-state) were combined. The periodicity of each unit cell remained constant.

As shown in figures 22(a) and (b), both 0-state and π-state unit cells were analysed. It was observed that the surface current directions in the 0-state and π-state unit cells were opposite to each other, confirming that mutual coupling and edge effects were minimal. The electric field and surface current distributions of individual unit cells are depicted in figures 22(a) and (b).

To understand mutual coupling and edge effects, we examined different arrangements of unit cells. First, we analysed a combination of two-unit cells.

In the first combination, figure 22(c) illustrates the π-state unit cells positioned along the horizontal axis. The electric field distribution indicates that mutual coupling was maximized due to the identical current

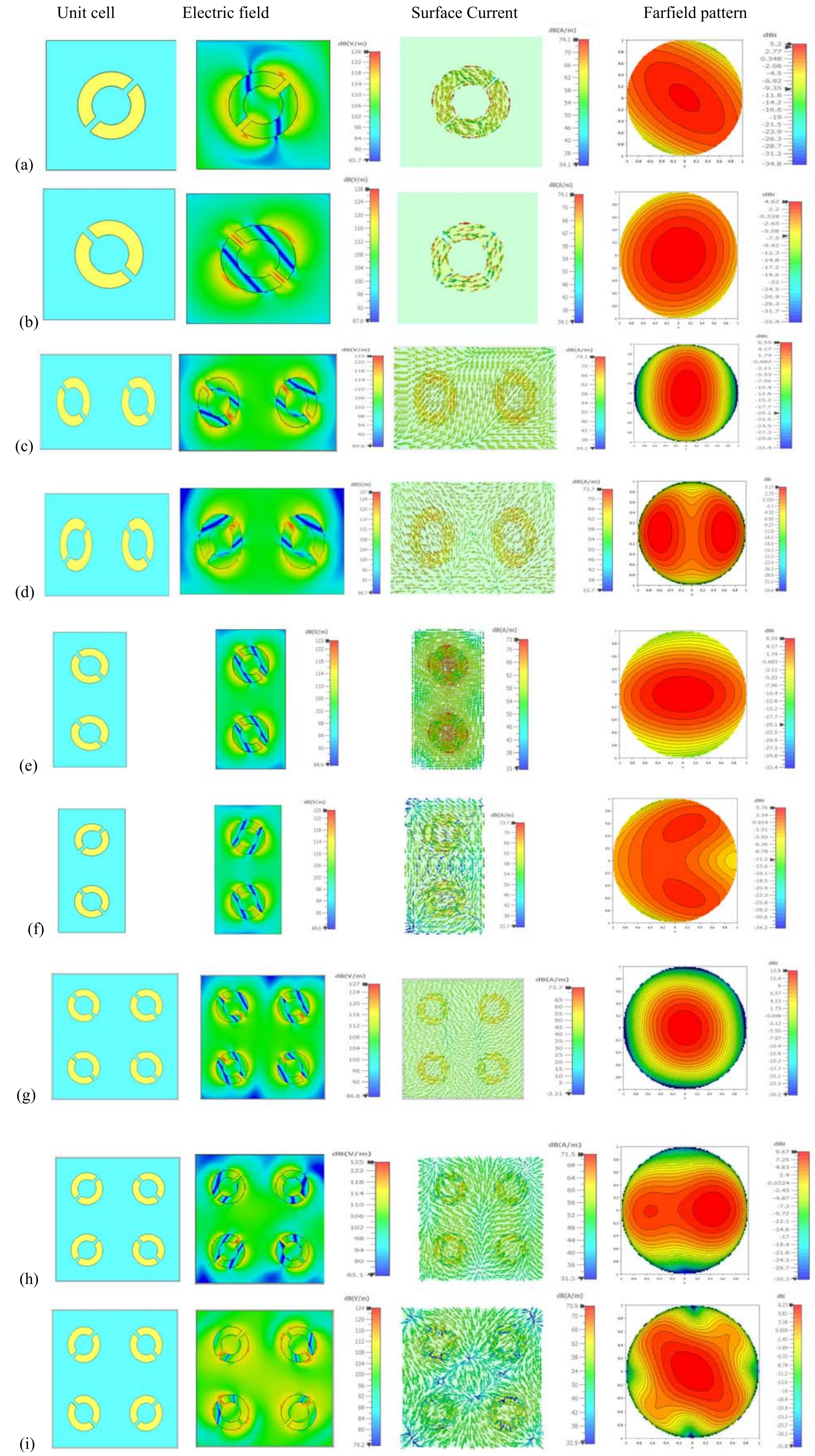

Figure 22. Mutual coupling analysis of different arrangement of unit cell.

direction in both unit cells. This observation is further supported by the realized gain plot, which shows a maximum gain of 6.59 dBi. However, the beam appeared broad. Based on these results, we concluded that mutual coupling reached its peak when both unit cells were in the same state.

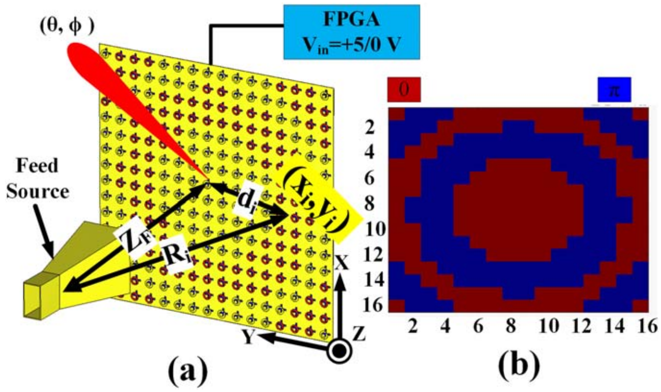

Figure 23. Schematic configuration of the array (a) 3D- view of array element (b) phase distribution of array element.

In the second combination, as shown in figure 22(d), both 0-state and π-state unit cells were arranged horizontally. The electric field and surface current distributions revealed that the unit cells had opposite surface current directions. This indicates that mutual coupling between them was minimal. As a result, two beams were obtained. The maximum realised gain is 5.17 dBi and beam is distinct which is less in comparison of first combination due to less mutual coupling.

In the third combination, as shown in figure 22(e), π-state unit cells were positioned along the vertical axis. The electric field distribution indicated that mutual coupling was maximized due to the identical current direction in both unit cells. This observation was further supported by the realized gain plot, which showed a maximum gain of 6.5 dBi. However, the beam appeared broad. Based on these results, we concluded that mutual coupling was maximized when both unit cells were in the same state.

In the Fourth combination, both 0-state and π-state unit cells were arranged vertically, as shown in figure 22(f). The electric field and surface current distributions revealed that the unit cells had opposite surface current directions. This indicates that mutual coupling between them was minimal. As a result, two beams were obtained. The maximum realised gain is 5.7 dBi and beam is distinct which is less in comparison of third combination due to less mutual coupling.

In fifth, sixth, seventh we have 2×2 array for analysing the mutual coupling and edge effect with different arrangement. In the fifth combination, all unit cells were in the 0-state, as shown in figure 22(g). It was observed that mutual coupling was maximum, as indicated by the electric field distribution and surface current distribution. Due to this strong mutual coupling, a broad beam was obtained with a gain of 13.8 dBi.

In the sixth combination, 0-state and π-state unit cells were arranged vertically along the horizontal direction. The first column consisted of 0-state unit cells, while the second column consisted of π-state unit cells, as shown in figure 22(h). Strong mutual coupling was observed in the vertical direction, whereas mutual coupling was weaker in the horizontal direction due to the orientation of the electric field and surface current. As a result of this mutual coupling pattern, the maximum beam direction tilted toward the π-state unit cells. The maximum gain was 9.67 dBi, which was lower than that of the fifth combination due to reduced mutual coupling between the different state unit cells.

In the seventh combination, similar unit cells were arranged diagonally, as shown in figure 22(i). The electric field and surface current distributions revealed that mutual coupling was strongest along the diagonal direction. In contrast, mutual coupling was weaker in the horizontal and vertical directions. As a result, the beam was directed toward the centre.The maximum realized gain was 8.23 dBi, with a broad beam.

4.2. 16 × 16 array elements

A complete array is designed and analyzed based on the proposed unit cell. Figures 23(a) and (b), displays the detailed constructions of a 16×16 array elements, placed in the XY- plane. The dimension of the reflectarray is $1600\,\mu\text{m} \times 1600\,\mu\text{m}$. A pyramidal horn antenna illuminates the array elements. The feed is placed for a -10 dB edge taper at (X_F, Y_F, Z_F) (0, 0, 1299 μm). The optimum Z_F/D ratio calculated by using the maximum aperture efficiency (η_a). D is the maximum dimension of the array. The aperture efficiency is the product of the spillover efficiency (η_s) and edge taper efficiency(η_t) where $\eta_a = \eta_s \times \eta_t$. The spillover efficiency and tapered efficiency is calculated by (13) and (14), [52].

$$\eta_s = 1 - \cos^{q_f+1}(\theta_0) \tag{13}$$

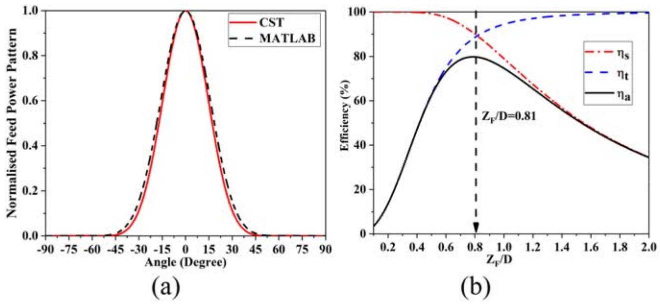

Figure 24. (a) Curve fitting of the normalized feed pattern in CST and MATLAB, (b) Aperture efficiency corresponding to the Z_F/D ratios.

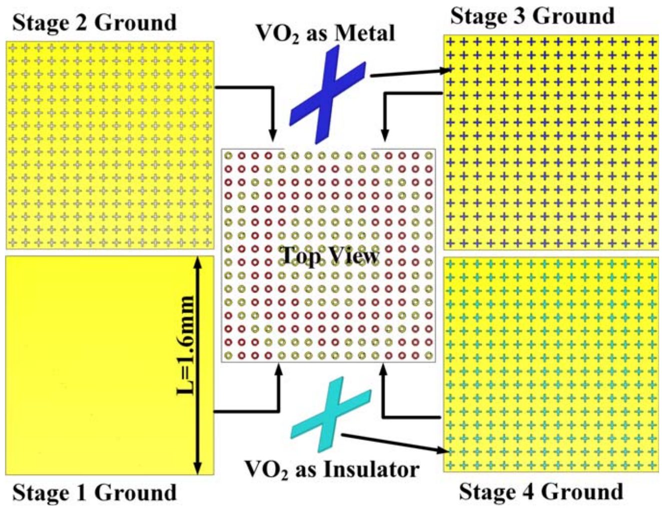

Figure 25. Configuration of the array design based on stages 1, 2, 3, and 4-unit cells.

$$\eta_t = \frac{2q_f\ (1 - \cos^{\left(\frac{q_f}{2}\right)-1}(\theta_0))^2}{\tan^2(\theta_0)\left(\frac{q_f}{2} - 1\right)^2(1 - \cos^{q_f}(\theta_0))} \tag{14}$$

The simulated feed power pattern with CST and MATLAB is shown in figure 24(a). The feed power pattern is calculated by using the equation of $\cos^{q_f}(\theta_0)$. For curve fitting the value of q_f is 13 for pyramidal horn antenna. The aperture efficiency for the value of q_f=13 is depicted in figure 24(b). The maximum aperture efficiency corresponding Z_F/D ratio is determined for q_f=13.

The required phase for each element is decided for −10 dB edge tapered feed and corresponding feed position (X_F, Y_F, Z_F) (0, 0, 1299 μm), which is given by (15), (16), [53, 54]

$$\phi(xi, yi) = -K_o(R_i - x_i \sin\theta \cos\phi + y_i \sin\theta \sin\phi) \tag{15}$$

$$\phi(xi, yi) = \begin{cases} 0 - state, & -90 \leqslant \phi(xi, yi) \leqslant 90^\circ \\ \pi - state, & Otherwise \end{cases} \tag{16}$$

Where, K_o is the wave number, Z_F is the distance between the phase center and the referenced element, and (x_i, y_i) is the position of each element in the XY-plane. R_i is the distance between *i*th element and phase center of the feed antenna. The direction of the collimated beam is defined by (θ, ϕ).

Figure 25 shows the configuration of the array for all four combinations of stages 1, 2, 3, and 4. The stage 1 array has a full ground plane and, in this case, it acts as a reflectarray, while in the stage 2, array has a cross-shaped slot on ground plane, and it acts as an FSS, FSS based cross polarized wave absorber and a reflective-transmittive surface. The stage 3 and stage 4 ground planes are obtained by changing the potential of the cross-shaped VO_2 film. The DC biasing is given to the VO_2 film by FPGA connected with the ground plane. If the potential is required biasing $+V_1$ voltage, the ground plane of stage 3 acts as metal and hence this array acts as a reflectarray, while if the potential is low (V_2; $V_2 < V_1$ Volt), the ground plane of stage 4 acts as FSS, FSS based cross polarized wave absorber and reflective-transitive surface. The performance characteristics of the four stages-based arrays are described in section IV.

5. Applications

5.1. Reflectarray antenna

The basic performance characteristic of the reflecting element is analyzed in stage 1 and stage 3 within sections II and III. The arrangement of the reflective element is displayed in figure 25. The array element is illuminated by pyramidal horn antenna of 13 dBi gain. The basic arrangement of the reflectarray element is in the XY-plane as shown in figure 23(a). The reflectarray is designed by using a wide band polarization rotating unit cell. The operating bandwidth of the array is 1.29 to 1.86 GHz (% BW = 36.1%).

The maximum efficiency of the proposed reflectarray at 1.5 THz in stage 1 is 22.12%. The simulated radiation pattern at 1.3 THz, 1.5 THz, and 1.7 THz for stage 1 and stage 3 is shown in figures 26(a) and (b), respectively. The simulated 3D-radiation patterns of the reflectarray antenna in UV-plane at 1.5 THz for stage 1 and stage 3 are shown in figures 27(a) and (b), respectively.

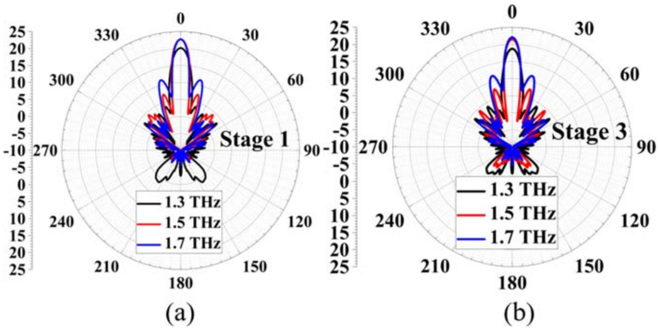

Figure 26. Simulated radiation patterns of the reflectarray antenna (a) stage 1 (b) stage 3.

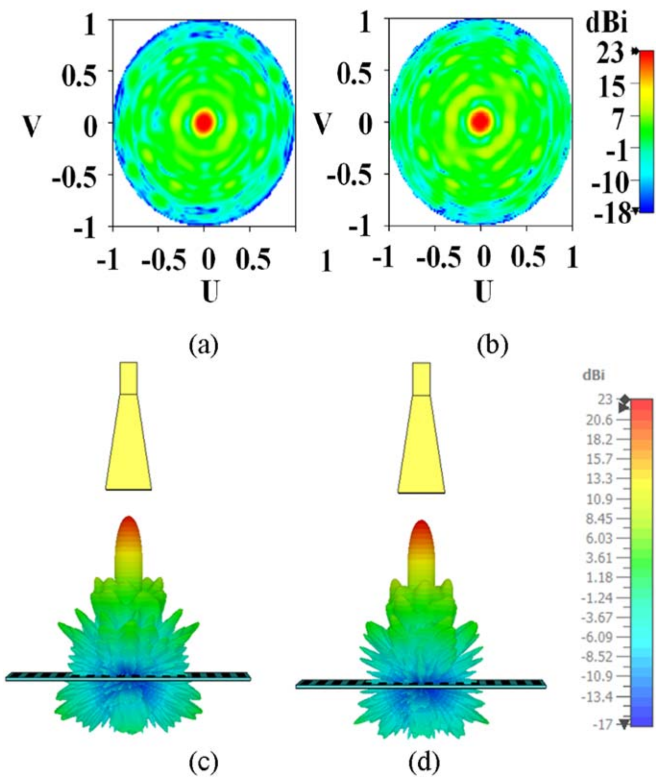

Figure 27. Simulated 3D-radiation patterns of the reflectarray antenna (a) in UV-plane at 1.5 THz for stage 1 (b) in UV-plane at 1.7 THz for stage 3. (c) in 3D at 1.5 THz for stage 1 (d)in 3D at 1.7 THz for stage 3.

5.2. Frequency selective surface

This section describes the proof of the concept for frequency selective surface of stage 2 and stage 4. In section II (B), the performance characteristics of the stage 2, FSS unit cell is described. In stage 2, it is observed that there are two narrow transmission bands that are separated by a wide stop band (1.4 THz–1.8 THz). Similarly, in stage 4, FSS also provides a stop band of (1.4 THz–1.7 THz). The stage 2 and stage 4 based array is illuminated by a pyramidal horn antenna, and then the response characteristics of the FSS array are obtained as shown in figures 28(a) and (b). The stage 2-based array acts as a band stop filter in the frequency band (1.4 THz–1.8 THz), while the stage 4-based array also acts as a band stop filter in the frequency band (1.4 THz–1.7 THz). The FSS based cross wave absorber is validated through the reduction of the reflective-transmittive gain in these stop bands. In comparison of the feed gain, the reflective-transmittive gain is less. The obtained gain is below 12 dBi, while the feed gain is 13 dBi. The simulated 3D-radiation patterns of frequency selective surface of stage 2 and stage 4 at 1.5 THz in UV-Plane and elevational-azimuth plane are shown in figures 29(a)–(d), respectively. The two narrow band reflective-transmission performance characteristics of the stage 2 and 4 based array are illustrated in section C.

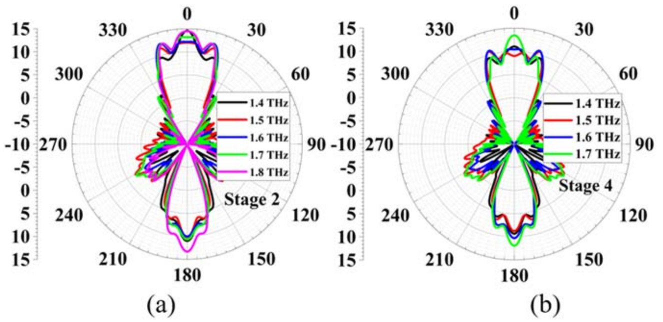

Figure 28. Simulated radiation patterns of the frequency selective surface (a) stage 2 (b) stage 4.

5.3. Reflective-transmittive surface

From section II (B) and (C), the stage 2, unit cell has the dual narrow transmission band with TB_1 (1.08–1.38 THz) and TB_2 (1.8–2.2 THz). While stage 4 has dual narrow transmission band of TB_1 (1.08–1.29 THz) and TB_2 (1.7 THz–2.2 THz).

In both transmission bands the reflective-transmittive nature of the unit cell is also described in sections II (D) and III (D) of stage 2 and stage 4, respectively. From section II(D), The performance characteristics of the stage 2-unit cell is used to design of reflective-transmittive surface. When it is illuminated by a feed antenna, then the surface will act as reflective-transmittive surface in the both bands TB_1 and TB_2. Which is validated in this section. Similar observation is found for the section III (D) unit cell based reflective-transmittive surface. The performance characteristics of both stage 2 and stage 4 based array is shown in figures 30(a) and (b). In figure 30(a), it is observed that stage 2-based reflective transmittive surface produces a high gain in both transmission bands. In transmission band TB_1 (at 1.1, 1.2, 1.3 THz), the reflective gain is about 16 dBi, while in TB_2 (at 1.9, 2, 2.1 THz), it is about 20 dBi, and the transmittive gain is about 15 dBi in TB_1 band while it is about 19 dBi in TB_2 band. From figure 30(b), it is observed that stage 4-based reflective transmittive surface produces high gain in both transmission bands. In transmission band TB_1 (at 1.1, 1.2, 1.3 THz), the reflective gain is about 15 dBi, while in TB_2 (at 1.8, 1.9, 2, 2.1 THz), it is about 20 dBi, and the transmittive gain is about 14 dBi in TB_1 band, while it is about 16 dBi in TB_2 band. The simulated 3D-radiation pattern of reflective-transmittive surface of stage 2 and stage 4 based array at 1.9 THz in UV-plane and elevation-azimuth plane is shown in figures 31(a)–(d), respectively.

The peak realized gain versus frequency plot for the stages 1, 2, 3 and 4 is shown in figure 32. The stage 1-based array acts as a reflectarray with a maximum gain of 22.5 dBi at 1.6 THz, and its 3-dB gain bandwidth is 0.57 THz in the working band from 1.29 to 1.86 THz. The stage 3-based array also acts as a reflective surface in the active band from 1.3–1.85 THz with a maximum gain of 22.5 dBi at 1.6 THz.The stage 2 and stage 4 based array produces two narrow transmission bands separated by a wide stop band. The stage 2-based reflection-transmission array 3-dB bandwidth of band 1 is 0.36 THz, while band 2 bandwidth is 0.32 THz. The stage 4-based reflection-transmission array 3-dB bandwidth of band 1 is 0.26 THz while band 2 bandwidth is 0.44 THz.

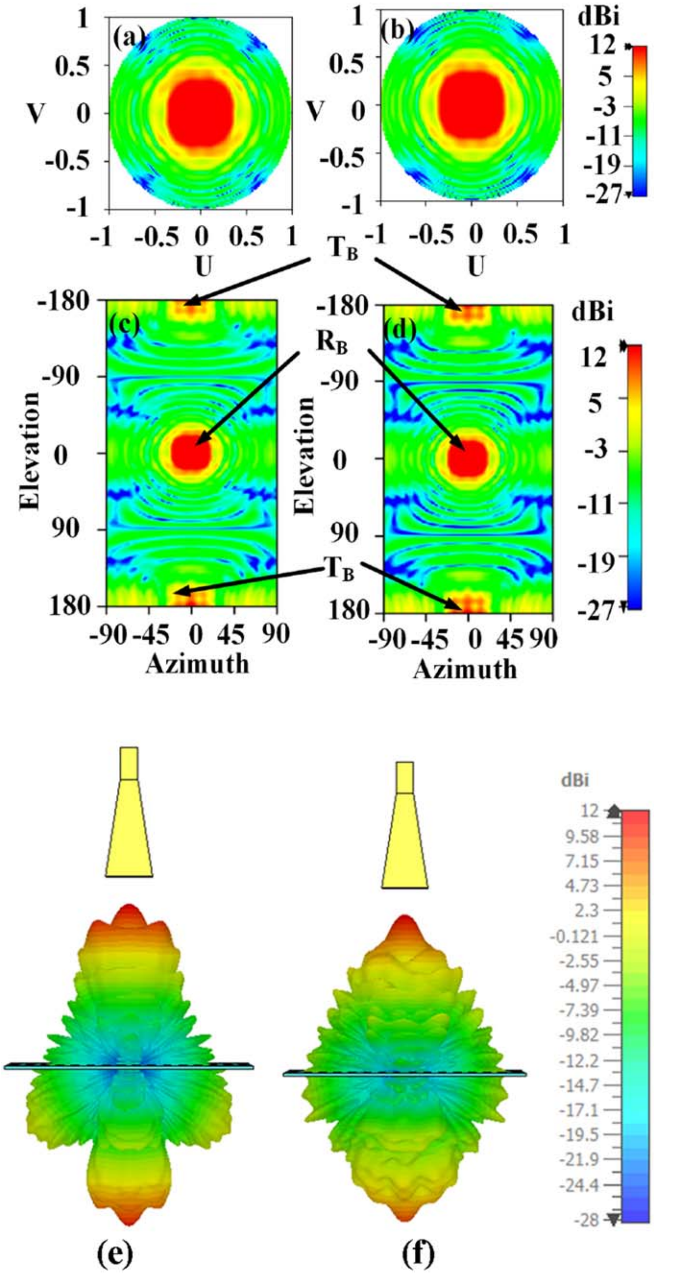

Figure 29. Simulated 3D-radiation patterns of frequency selective surface of stage 2 and stage 4 at 1.5 THz in (a) UV-plane stage 2, (b) UV-plane stage 4 (c) elevation-azimuth plane stage 2, (d) elevation-azimuth plane stage 4. (e) 3D- plane at stage 2 (f) 3D-.

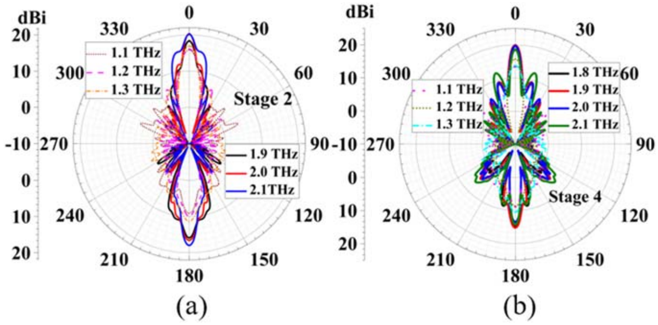

Figure 30. Simulated radiation pattern of the transmittive-reflective surface (a) stage 2 (b) stage 4.

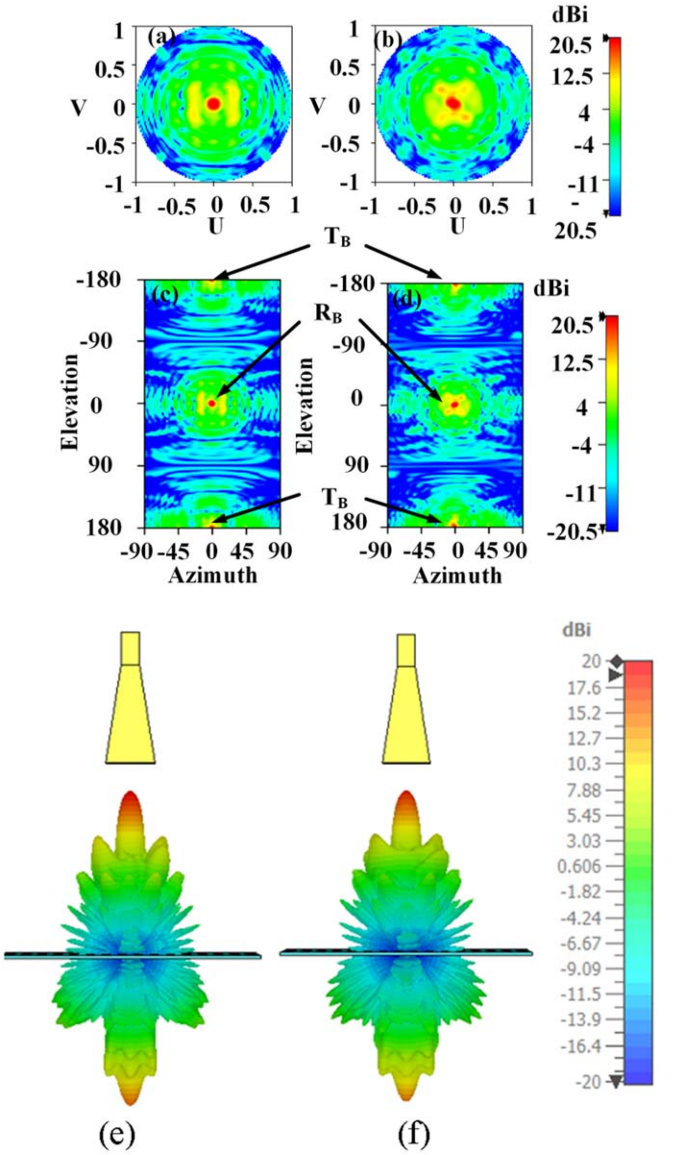

Figure 31. Simulated 3D-radiation patterns of the reflective-transmitive surface of stage 2 and stage 4 at 1.9 THz (a) UV- plane stage 2 (b) UV- plane stage 4 and (c) elevation-azimuth plane stage 2, (d) elevation-azimuth plane stage 4. (e)3D-radiation pattern at stage 2, (d) 3D-radiation pattern at stage 4.

R^1_{BW}: stage 1 reflectarray bandwidth, R^3_{BW}: stage 3 reflectarray bandwidth, RT^2_{BW1}: stage 2 reflect-transmit array bandwidth of band 1, RT^2_{BW2}: stage 2 reflect-transmit array bandwidth of band 2, RT^4_{BW1}: stage 4 reflect-transmit array bandwidth of band 1, RT^4_{BW2}: stage 4 reflect-transmit array bandwidth of band 1.

The performance of the tri-function array is summarized in table 1.

6. Application scenario

The future application of this proposed work is shown in figures 33(a)–(c). To established the communication between the earth station and the moon satellite. In figure 33(a), the communication between earth station and a near earth orbit satellite will be established using the proposed reflectarray operating at 1.5 THz. However, the reflectarray will be unable to directly communicate with the moon satellite on the back side. However, if the information is converted into lowest 1.2 THz and highest 1.9 THz frequency the communication will be establish between both satellite when proposed work as reflective-transmittive surface which is shown in figure 33(b). However, in figure 33(c), when the 1.5 THz signal is transmitted by reflectarray from the earth, the information will be transmitted to the satellite near the earth, which convert the signal into 1.2/1.9 THz and the proposed array work as reflect-transmit array to communicate to the moon satellite, while the array absorbed the 1.5 THz signal at this time from earth station.

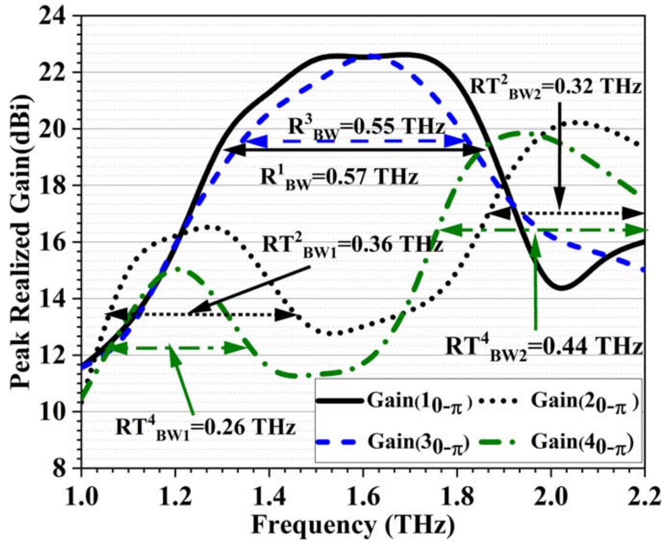

Figure 32. Gain versus frequency characteristics of the proposed array of stages 1, 2, 3 and 4.

Table 1. Comparative analysis with existing works.

References	Operating frequency (THz)			Gain (dBi)			Size (mm^2)	Efficiency (%)
	RA	RTA RT_{F1}/RT_{F2}	FSS Stop Band	RA	RTA RT_{F1}/RT_{F2}	FSS Stop Band (Absorber)		
[17]	0.875	—	0.9	22		—	5.76	
[19]	—	0.00475/0.01375	0.01	—	—	—	—	—
[22]	—	0.0058/0.0124	0.01	—	—	—	—	—
[27]	3	—	—	—	—	1.8	0.32	—
[31]	0.75	—	—	—	—	—	51.84	—
[33]	0.358	—	—	—	—	—	11.9	—
[35]	1.1	—	—	24	—	—	3.1	21
[55]	0.3	—	—	20	—	—	1369	0.5
[56]	0.21	—	—	—	—	—	58.98	—
[57]	—	6	—	—	24.4/22		.132	41/23
[58]	0.39			32.4			309.15	26
[59]	1	—	—	33.4	—	—	81	19
[60]	—	TA (0.9)	—	—	TA (35.96)	—	147.87	23
[61]	—	TA (0.34)	—	—	TA (34.90)	—	2733.97	7
[62]	—	TA (0.14)	—	—	TA (33.12)	—	1600	46
[63]	—	TA (0.27)	—	—	TA (20.8)		669.67	1.7
[64]	1.35	—	—	28	—	—	9	35
[65]	0.140			31.40			1089	46
[66]	3.6	—	—	20	—	—	0.298	19
[67]	0.102						1.38	28
	VO_2 (Metal)	**1.5**	**—**	**22.5**		**—**	**2.56**	**22.14**
This Work	VO_2 (Insulator)	—	1.2/ 1.9	1.5	16.5/15		2.56	8.6/2.4
					20/19.5	12		19.43/17.32

FSS: Frequency Selective Surface, TA: Transmitarray, RT_{F1} and RT_{F2}: Reflection Transmission Frequency, RA: Reflectarray, RTA: Reflect-transmit array.

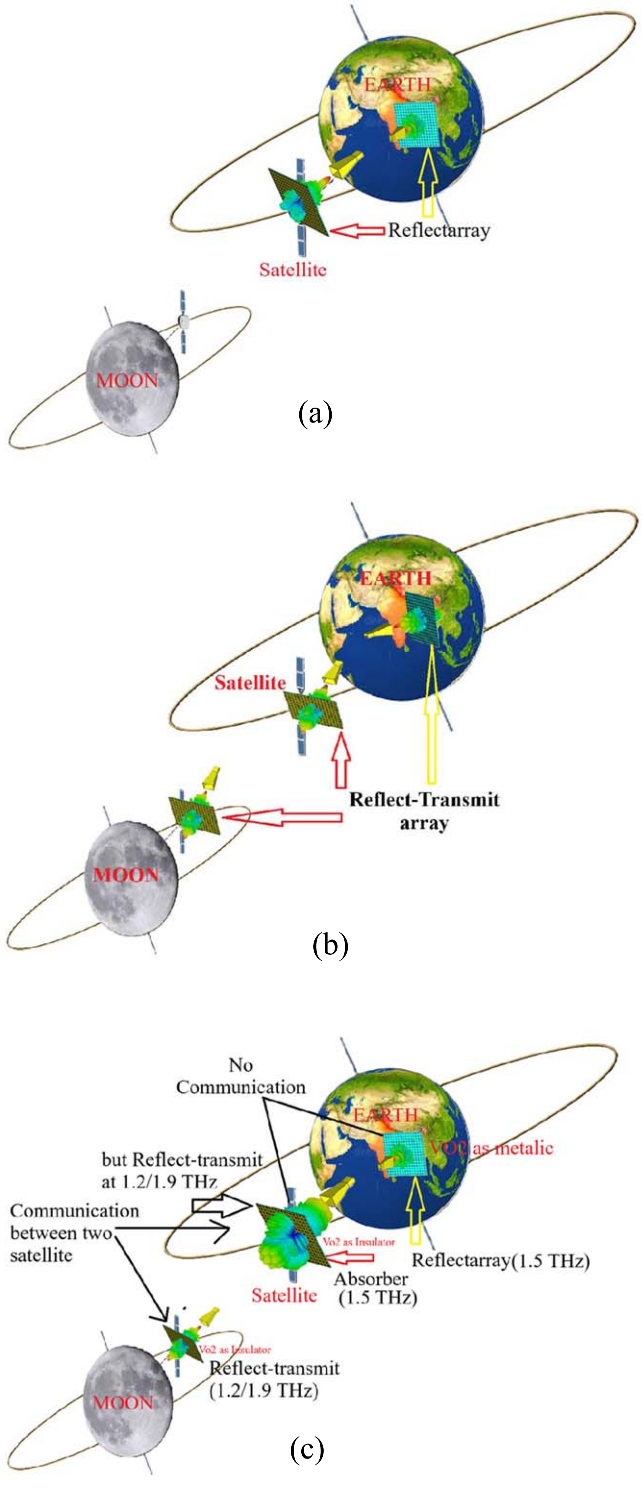

Figure 33. Application of the proposed work. (a) Reflectarray used to communication between satellite and earth station. (b) Reflect-transmit array communicates between moon satellite to earth satellite and to the earth station. (c) Communication established between earth station to the near-earth orbit satellite using 1.5 THz frequency when the VO_2 as metallic state and when the VO_2 as insulator then it's used as absorber at 1.5 THz frequency and reflect-transmit at 1.2/1.9 THz between the near earth orbit satellite to moon satellite.

7. Conclusion

In this paper, a novel quad-function unit cell and16 $\times$ 16 array based on intelligent ground plane is presented. The intelligent ground plane is designed by etching a cross-shaped slot on the gold ground plane which is filled by a thin VO_2 film. The quad-function of the unit cell and array is obtained by changing the applied potential to the VO_2 film. The unit cell performs a reflective element when the applied potential is high ($+V_1$ Volt), because the conductivity ($\sigma = 2 \times 10^5\ S\ m^{-1}$) of the VO_2 film is very high at the temperature above 341.15 K. The performance of unit cell is validated through the design of array, which acts as a high gain wideband reflectarray at this potential. The unit cell performs a frequency selective surface with two narrow-band transmissions, which is separated by a wide stop band. It is possible because the conductivity of the VO_2 film changes from high ($\sigma = 2 \times 10^5$ S m^{-1}) to low ($\sigma = 200$ S m^{-1}) by changing the potential from $+V_1$ Volt (High) to V_2 Volt (Low). The performance of the FSS is also validated through the design array. When the array is illuminated by horn antenna, the reflective gain is very low in the stop band while the reflective-transmittive gain is above the feed gain that confirms the FSS array produces two narrow transmission bands which are separated by a wide stop band. In these two narrow transmission bands, the array performs a reflective-transmittive surface, which is also validated by the performance of the unit cell as well as the array. The array provides a high gain in these two bands of the reflective and transmittive beam. The 3-dB bandwidth of the reflectarray is 0.57 THz with the metal (gold) ground plane and 0.55 THz with intelligent ground plane with high gain of 22.5 dBi and the aperture efficiency is 22.12%.

The transmission band is TB_1 (1.08 to 1.29 THz) and TB_2 (1.81–2.2 THz) while the stop band is (1.29–1.81THz). The transmittive gain is obtained in band 1 is about 16.5 dBi while in band 2, it is about 20 dBi. In stop band, the gain is 12 dBi. It is concluded that, in this article all the four behaviors are obtained in a single array using intelligent ground plane and this array can be utilized for future 6G and satellite applications.

Acknowledgments

This work is supported by the Science Engineering Research Board, Govt of India, as sponsored research project number EEQ/2021/000588 and ISRO/RAC-S/IIT(BHU)/2022-23, respectively. One of the authors, Ravi Mali, is thankful to the Science Engineering Research Board, Govt. of India for providing financial support in the form of a Junior Research Fellowship.

Data availability statement

The data that support the findings of this study are available upon reasonable request from the authors. The data that support the findings of this study are available upon reasonable request from the authors.

ORCID iDs

Ravi Mali https://orcid.org/0000-0002-3320-7978
Rajkumar Jatav https://orcid.org/0000-0001-8258-0261
Praveen Singh Rathore https://orcid.org/0000-0002-3364-4190
Manoj Kumar Meshram https://orcid.org/0000-0002-0940-316X

References

[1] Alsaedi W K, Ahmadi H, Khan Z and Grace D 2023 Spectrum options and allocations for 6G: a regulatory and standardization review *IEEE Open Journal of the Communications Society* **4** 1787–812
[2] Ginn J C, Lail B A and Boreman G D 2007 Phase characterization of reflectarray element at infrared *IEEE Transaction on Antennas and Propagation* **55** 2989–93
[3] Headland D, Niu T, Carrasco E, Abbott D, Sriram S, Bhaskaran M, Fumeaux C and withayachumnankul W 2017 Terahertz reflectarrays and nonuniform metasurfaces *in IEEE Journal of Selected Topics in Quantum Electronics* **23** 1–18
[4] Carrasco E and Perruisseau-Carrier J 2013 Reflectarray antenna at terahertz using graphene *IEEE Antennas Wirel. Propag. Lett.* **12** 253–6
[5] Chang Z, You B, Wu L S, Tang M, Zhang Y P and Mao J F 2016 A reconfigurable graphene reflectarray for generation of vortex THz waves *IEEE Antennas Wirel. Propag. Lett.* **15** 1537–40
[6] Shi Y and Zhang Y 2018 Generation of wideband tunable orbital angular momentum vortex waves using graphene metamaterial reflectarray *IEEE Access* **6** 5341–7
[7] Soleimani H and Oraizi H 2021 Programmable terahertz vortex beam reflectarray antenna based on a graphene phoenix unit cell *J. Phys. D: Appl. Phys.* **54** 165302
[8] Meng X, Nekovee M and Wu D 2021 The design and analysis of electronically reconfigurable liquid crystal-based reflectarray metasurface for 6G beamforming, beamsteering, and beamsplitting *IEEE Access* **9** 155564–75
[9] Kim H, Kim J and Oh J 2022 Communication a novel systematic design of high-aperture-efficiency 2D beam-scanning liquid-crystal embedded reflectarray antenna for 6G FR3 and radar applications *IEEE Trans. Antennas Propag.* **70** 11194–8
[10] Adatia N A R A W 1978 Offset-parabolic-reflector antennas: a review *Proc. IEEE* **66** 1592–618
[11] Li W, Gao S, Zhang L, Luo Q and Cai Y 2018 An ultra-wide-band tightly coupled dipole reflectarray antenna *IEEE Trans. Antennas Propag.* **66** 533–40
[12] Jatav R K, Mali R, Rathore P S and Meshram M K 2024 An X-band beam-scanning reflectarray antenna stimulated using a spoof surface plasmon polaritons based low profile endfire MIMO antenna *AEU Int J Electron Communication* **183** 1553801–8

[13] Tiwari S, Singh A K and Dubey A 2024 Wide-band wide-angle beamsteerable meta-lens antenna for terrestrial/nonterrestrial 5G communication systems *IEEE Journal on Miniaturization for Air and Space Systems* **5** 117–24
[14] Malhat H A E A, Deen S Z and Gaber S 2014 Graphene based transmitarray for terahertz applications *Progress In Electromagnetics Research M* **36** 185–91
[15] Liu G, Wang H, Jiang J and Xue F 2016 Terahertz substrateless transmitarray antenna design and microfabrication *Microwave Optical Technology Letter* **58** 2096–100
[16] Zainud-Deen S H ,, Hassan W M and Malhat H A 2015 Bi-function multi-beam graphene lense antenna for terahertz applications *Wireless Engineering and Technology* *7* 36–45
[17] Chen L, Qu S W, Chen B J, Bai X, Ng K B and Chan C H 2017 Terahertz metasurfaces for absorber or reflectarray applications *IEEE Trans. Antennas Propag.* **65** 234–41
[18] Du X, Yan F, Wang W, Zhang L, Bai Z, Zhou H and Hou Y 2021 A broadband switchable metamaterial absorber/reflector based on multi-laps graphene sheets in the terahertz band *IEEE Photonics J.* **13** 1–8
[19] Lockyer D S, Vardaxoglou J C and Simpkin R A 2000 Complementary frequency selective surfaces *IEEE Proceedings - Microwaves, Antennas and Propagation* **8** 501–7
[20] Munk B A , 2000 *Frequency Selective Surfaces—Theory and Design* (Wiley)
[21] Kim S M, Leite C M, Park J Y, Kim H J and Jang J H 2020 Multiband terahertz self-complementary metasurface *IEEE Access* **8** 199051–9
[22] Kanth V K and Raghavan S 2018 Equivalent circuit analysis of complementary FSS for selective EM shielding *2018 15th Int. Conf. on Electro Magnetic Interference & Compatibility (INCEMIC)* 1–4
[23] Kiani G I, Ford K L, Esselle K P, Weily A R and Panagamuwa C J 2007 Oblique incidence performance of a novel frequency selective surface absorber *IEEE Trans. Antennas Propag.* **55** 2931–4
[24] Areias T C, Carvalho R N G, da Silva M W B, Matos L J, Neto J J G P, Campos A L P S and Neto A G 2020 Frequency selective surface microwave absorber for WLAN applications *Journal of Communication and Information System* **35** 208–16
[25] Zhang Y *et al* 2024 Development of a multifunctional terahertz metasurface for simultaneous broadband absorption, polarization conversion, and wavefront manipulation *Eur. Phys. J. Plus* **139** 765
[26] Gao J *et al* 2024 A vanadium dioxide-based thz metasurface for dual-function switching between wideband absorption and polarization conversion *J. Electron. Mater.* **53** 8180–9
[27] Lian X, Ma m, Tian J and Yang R 2023 Study on a bifunctional switchable metasurface with perfect absorption and polarization conversion based on VO2 and graphene in THz region *Diam. Relat. Mater.* **136** 1100601–10
[28] Fu C, Zhang L, Zhang Y, Li N, Gu S, Ju J, Pan R, Liu X and Han L 2024 Bifunctional flexible metasurface based on graphene and vanadium dioxide for polarization conversion and absorption *Diam. Relat. Mater.* **142** 110862
[29] Varshney A K, Pathak N P and Sircar D 2022 Low-profile frequency reconfigurable graphene-based dipole antennas loaded with wideband metasurface for THz applications *Plasmonics* **17** 2351–63
[30] Dash S and Patnaik A 2018 Performance of graphene plasmonic antenna in comparison with their counterparts for low-terahertz applications *Plasmonics* **13** 2353–60
[31] Xu G, Li Q, Su H, Huang H and Wang S 2024 VO2-based metasurface for dynamically tenable terahertz surface plasmonic waves *Material Research Express* **11** 075801
[32] Wu Y, Tao W, Zhao F, Li C, Fang B, Zhang P, Hong Z, Jing X and Yua M 2024 Review for metamaterials and metasurface based on vanadium dioxide phase change materials *Opt. Laser Technol.* **179** 111376
[33] Song T *et al* 2025 Terahertz coding metasurface with low-switch-ratio for rapid 1-bit phase modulation and beam steering *ACS Photonics* **12** 952–62
[34] Dalal K and Sharma Y 2025 VO2 based polarization-independent dual-wavelength plasmonic switches using U and C shaped nanostructures. *Sci. Rep.* **15** 4020
[35] Qureshi S A, Kamarudin M R, Abbasi M I, Yamada Y, Dahri M H, Abidin Z Z and Ramli N 2024 The 6G reconfigurable reflectarray antenna using a gold-VO_2 bilayer structure *Progress In Electromagnetics Research M* **130** 63–70
[36] Kumar S, Pickett M D, Strachan J P, Gibson G, Nishi Y and Williams R S 2013 Local temperature redistribution and structural transition during joule-heating-driven conductance switching in VO2 *Advanced Material* **25** 6128–32
[37] Li D, Sharma A A, Gala D K, Shukla N, Paik H, Datta S, Schlom D G, Bain J A and Skowronski M 2016 Joule heating-induced metal–insulator transition in epitaxial VO2/TiO2 devices *ACS Applied Material Interfaces* **8** 12908–14
[38] Wu B, Zimmers A, Aubin H, Ghosh R, Liu Y and Lopez R 2011 Electric field-driven phase transition in vanadium dioxide *Physics. Review applied. B* **84** 2414101–4
[39] Shi Y and Chen L Q 2019 Current-driven insulator-to-metal transition in strongly correlated VO2 *Physics Review applied* **11** 014059
[40] Li H, Xu W, Cui Q, Wang Y and Yu J 2020 Theoretical design of a reconfigurable broadband integrated metamaterial terahertz device *Opt. Express* **28** 40060–74
[41] Wang S, Kang L and Werner D H 2017 Hybrid resonators and highly tunable terahertz metamaterials enabled by vanadium dioxide (VO2) *Scientific Report* **7** 1–8
[42] Mali R, Jatav R, Rathore P S, Bharati R and Meshram M K 2023 High gain wideband 16 × 16 reflectarray antenna for 5G and mm-wave Application *2023 IEEE Microwaves, Antennas, and Propagation Conf. (MAPCON)*
[43] Costa F 2021 A Simple Effective Permittivity Model for Metasurfaces Within Multilayer Stratified Media *IEEE Transactions on Antennas and Propagation* **69** 5148–53
[44] Wakatsuchi H, Paul J and Christopoulos C 2012 Performance of Customizable Cut-Wire-Based Metamaterial Absorbers: Absorbing Mechanism and Experimental Demonstration *IEEE Transactions on Antennas and Propagation* **60** 5743–52
[45] Gao X, Han X, Cao W-P, Li H O, Ma H F and Cui T J 2015 Ultrawideband and High-Efficiency Linear Polarization Converter Based on Double V-Shaped Metasurface *IEEE Transactions on Antennas and Propagation* **63** 3522–30
[46] Huang H, Xia H, Xie W, Guo Z, Li H and Xie D 2018 Design of broadband graphene-metamaterial absorbers for permittivity sensing at mid-infrared regions *Scientific Reports* **8** 1–10
[47] Srivastava S K and Meshram M K 2024 Comments on 'Analysis and Design of Three-Layer Perfect Metamaterial-Inspired Absorber Based on Double Split-Serration-Rings Structure' *IEEE Transactions on Antennas and Propagation* **72** 3854–57
[48] Srivastava S K, Dubey R and Meshram M K 2023 Design, Modeling and Analysis of Low Cross Polarization Level Low Radar Cross Section Conformal Ultra Wideband Absorber based on Resistive Metasurface *Progress In Electromagnetics Research M* **121** 147–56
[49] Milon M.A 2006 Analysis of mutual coupling for the simulation of reflectarrays radiating cells *2006 First European Conference on Antennas and Propagation (France)*
[50] Jamaluddin M H, Gillard R, Sauleau R and Milon M-A 2009 Perturbation Technique to Analyze Mutual Coupling in Reflectarrays *IEEE Antennas and Wireless Propagation Letters* **8** 697–700

[51] Milon M.A 2006 Analysis of mutual coupling for the simulation of reflectarrays radiating cells *2006 First European Conference on Antennas and Propagation (France)*
[52] Pozar D M, Targonski S D and Syrigos H D 1997 Design of millimeter wave microstrip reflectarrays *IEEE Transactions on Antennas and Propagation* **45** 287–96
[53] Huang J 2008 *Rflectarray Antenna* (Wiley)
[54] Mali R and Meshram M K 2022 Design A 1-bit high gain 21 × 21 reconfigurable reflectarray antenna for X-band applications *in 2022 IEEE Microwaves, Antennas, and Propagation Conference (Banglore)*
[55] Ali A, Khalily M, Brown T and Tafazolli R 2022 Metasurface-based THz reflectarray antenna with vortex multiplexing and beam-steering capabilities for future wireless communications *iScience* **25** 104725
[56] Yang D, Wang W, Lv E, Wang H, Liu B, Hou Y and Chen J H 2022 Programmable VO2 metasurface for terahertz wave beam steering *iScience* **25** 104824
[57] Zainud-Deen S H, Hassan W M and Malhat H A 2016 Bi-Function Multi-Beam Graphene Lens Antenna for Terahertz Applications *Wireless Engineering and Technology* **07** 36–45
[58] Miao Z W, Hao Z C, Wang Y, Jin B B, Wu J B and Hong W 2019 A 400-GHz High-Gain Quartz-Based Single Layered Folded Reflectarray Antenna for Terahertz Applications *IEEE Transactions on Terahertz Science and Technology* **9** 78–88
[59] Zhu S Y, Wu G B, Pang S W and Chan C H 2021 Compact Terahertz Dielectric Folded Metasurface *Advanced Optical Materials* **10** 2101663
[60] Miao Z-W, Liu Z, Hao Z-C, Zeng Y, Zhu D, Zhao J-H, Ding C-Y, Cheng L, Zhao L and Hong W 2024 A 1.0-THz High-Gain Metal-Only Transmit-Array Antenna Based on High-Precision UV-LIGA Microfabrication Technology *IEEE Transactions on Terahertz Science and Technology* **14** 269–282
[61] Liu G, Wang H, Jiang J and Xue F 2016 Terahertz substrateless transmitarray antenna design and microfabrication *Microwave and Optical Technology Letters* **58** 2096–2100
[62] Miao Z W, Hao Z C, Luo G Q, Gao L, Wang J, Wang X and Hong W 2018 140 GHz High-Gain LTCC-Integrated Transmit-Array Antenna Using a Wideband SIW Aperture-Coupling Phase Delay Structure *IEEE Transactions on Antennas and Propagation* **66** 182–90
[63] Xu J, Chen Z N and Qing X 2013 270-GHz LTCC-Integrated High Gain Cavity-Backed Fresnel Zone Plate Lens Antenna *IEEE Transactions on Antennas and Propagation* **61** 1679–87
[64] Mali R, Jatav R, Rathore P S and Meshram M K 2024 A wide-band high gain beamsteerable variable patch reflectarray antenna for THz applications *Optik* **311** 171915
[65] He X, Yang W, Liao S, Li Y, Xue Q and Che W 2024 140-GHz High-Efficiency Low-Profile Reflectarray Antenna Using Heterogeneous Design Strategy *IEEE Transactions on Antennas and Propagation* **72** 932–37
[66] Gaber S M, Abdelghany M A and Ibrahim A A 2024 Reflectarray with Graphene and beam steering feature for terahertz communication *Journal of Optics* **0** 1–8
[67] Zhou Y, Ma X, Luo Q, Ma Y, Alexandropoulos G C and Yang X 2024 Wideband Sub-THz Reconfigurable Intelligent Surface Using Planar Tightly Coupled Dipoles *IEEE Antennas and Wireless Propagation Letters* **23** 3659–63